An analysis of large HNO_3-containing particles sampled in the Arctic stratosphere during the winter of 1999/2000

M. J. Northway,[1,2,3] R. S. Gao,[1] P. J. Popp,[1,2] J. C. Holecek,[1,2] D. W. Fahey,[1,2] K. S. Carslaw,[4] M. A. Tolbert,[2,3] L. R. Lait,[5] S. Dhaniyala,[6] R. C. Flagan,[6] P. O. Wennberg,[6] M. J. Mahoney,[7] R. L. Herman,[7] G. C. Toon,[7] and T. P. Bui[8]

Received 9 July 2001; revised 28 November 2001; accepted 1 December 2002; published 24 October 2002.

[1] Large (>2 μm diameter) HNO_3-containing polar stratospheric cloud (PSC) particles were measured in situ by the NOAA NO_y instrument on board the NASA ER-2 aircraft during seven flights in the 1999/2000 Arctic winter vortex. Here we discuss the detection of these large PSC particles, their spatial distribution, the ambient conditions under which they were detected, and our methods for interpreting NO_y time series with respect to particle sizes and number concentrations. The particles were observed through the use of two NO_y inlets on a particle separator extending below the ER-2 aircraft. The particle phase is assumed to be nitric acid trihydrate (NAT) or nitric acid dihydrate (NAD). Over a 48-day period, particles were sampled in the Arctic vortex over a broad range of latitudes (60–85°N) and altitudes (15–21 km). Typically, regions of the atmosphere up to 4 km above the observed large particle clouds were saturated with respect to NAT. Occasionally, large particles were measured in air subsaturated with respect to NAT, suggesting ongoing particle evaporation. Vortex minimum temperatures in the observation period suggest that synoptic-scale ice saturation conditions are not required for the formation of this type of particle. Three analytical methods are used to estimate size and number concentrations from the NO_y time series. Results indicate particle sizes between 5 and 20 μm diameter and concentrations from 10^{-5} to 10^{-3} cm^{-3}. These low number concentrations imply a selective nucleation mechanism. Particle sizes and number concentrations were greater during the midwinter flights than the late winter flights. Knowledge of the geographical extent of large particles, actual sampling conditions, and particle size distributions offers multiple constraints for atmospheric models of PSC formation, which will lead to a better understanding of the process of denitrification and improvements in modeling future ozone loss. *INDEX TERMS:* 0305 Atmospheric Composition and Structure: Aerosols and particles (0345, 4801); 4801 Oceanography: Biological and Chemical: Aerosols (0305); 0320 Atmospheric Composition and Structure: Cloud physics and chemistry; 0340 Atmospheric Composition and Structure: Middle atmosphere—composition and chemistry; 0345 Atmospheric Composition and Structure: Pollution—urban and regional (0305); *KEYWORDS:* polar stratospheric clouds, particles, denitrification, HNO_3, NAT, NO_y

Citation: Northway, M. J., et al., An analysis of large HNO_3-containing particles sampled in the Arctic stratosphere during the winter of 1999/2000, *J. Geophys. Res.*, *107*(D20), 8289, doi:10.1029/2001JD001079, 2002.

1. Introduction

[2] Since the 1980s nitric acid (HNO_3)-containing polar stratospheric cloud (PSC) particles have been recognized to play a key role in the wintertime ozone (O_3) destruction of the Antarctic and Arctic stratospheres [*Peter*, 1997]. First, PSC cloud particles provide sites for the heterogeneous reactions that convert inactive chlorine to active chlorine [*Solomon et al.*, 1986]. Second, the sedimentation of HNO_3-containing particles irreversibly removes reactive nitrogen in the form of HNO_3 from air parcels in a process known as denitrification [*Toon et al.*, 1986]. In a denitrified atmosphere, chlorine remains in its active forms longer and causes more ozone destruction. Although denitrification has been observed extensively in both polar vortices using both in situ [*Fahey et al.*, 1990; *Popp et al.*, 2001] and remote [*Santee et al.*, 1995; *Dessler et al.*, 1999; *Kondo et al.*, 2000; *Kleinböhl et al.*, 2002] techniques, important details of the process are still not well understood. In particular, our ability to predict denitrification accurately in ozone loss

[1]NOAA Aeronomy Laboratory, Boulder, Colorado, USA.
[2]Cooperative Institute for Research in Environmental Sciences, University of Colorado, Boulder, Colorado, USA.
[3]Department of Chemistry and Biochemistry, University of Colorado, Boulder, Colorado, USA.
[4]School of the Environment, University of Leeds, Leeds, UK.
[5]NASA Goddard Space Flight Center, Greenbelt, Maryland, USA.
[6]California Institute of Technology, Pasadena, California, USA.
[7]Jet Propulsion Laboratory, California Institute of Technology, Pasadena, California, USA.
[8]NASA Ames Research Center, Moffett Field, California, USA.

0148-0227/02/2001JD001079$09.00

models has long been impeded by unanswered questions about PSC composition, nucleation mechanisms, and size.

[3] PSC composition is categorized as type I (containing HNO_3) or type II (containing primarily water ice) [*Poole and McCormick*, 1988]. Laboratory data have identified three compositions for type I PSCs: supercooled ternary solution (STS) containing HNO_3, sulfuric acid (H_2SO_4), and water (H_2O) [*Molina et al.*, 1993; *Zhang et al.*, 1993]; solid nitric acid trihydrate ($HNO_3 \cdot 3H_2O$) (NAT) [*Hanson and Mauersberger*, 1988]; and solid nitric acid dihydrate ($HNO_3 \cdot 2H_2O$) (NAD) [*Worsnop et al.*, 1993]. However, defining the roles of these PSC types in and near the edges of the polar vortices has been limited by a lack of appropriate observations. Only recently have in situ observations confirmed the composition of liquid [*Schreiner et al.*, 1999] and solid [*Voigt et al.*, 2000] nitric acid phases in PSCs. In most observations of type I PSCs, particles have relatively small sizes (<2 μm diameter) and large total number densities (>1 cm^{-3}). Modeling studies have identified many of these high number density populations as STS particles [*Carslaw et al.*, 1994; *Drdla et al.*, 1994; *Del Negro et al.*, 1997].

[4] A principle factor in understanding denitrification is the nucleation mechanism for each PSC phase. STS particles grow by condensation of HNO_3 and H_2O on background stratospheric nuclei (1–10 cm^{-3}) [*Wilson et al.*, 1990; *Deshler and Oltmans*, 1998], as ambient temperatures decrease below 200 K [*Carslaw et al.*, 1997]. This process is not impeded by a nucleation barrier, so all nuclei generally activate. Particle sizes are limited to less than about 2 μm diameter by available HNO_3 and H_2O. Therefore STS particles have low fall velocities and are not effective at denitrifying the stratosphere [*Tabazadeh et al.*, 2000]. Conversely, the nucleation mechanisms for NAT and NAD are not well understood [*Peter*, 1997; *Zondlo et al.*, 2000]. Laboratory studies have shown that both NAD and NAT formation have nucleation barriers [*Worsnop et al.*, 1993]. A number of studies have proposed that populations of large (>2 μm) NAT or NAD particles would have strong potential to denitrify parcels on the timescale of days [*Salawitch et al.*, 1989; *Toon et al.*, 1990; *Waibel et al.*, 1999]. Because of the limited amount of HNO_3 in the stratosphere, a selective nucleation mechanism is typically invoked to explain the limitation of particle concentrations to much less than the background nuclei concentrations [*World Meteorological Organization* (*WMO*), 1999]. Several theories such as the slow freezing of background particles to form nitric acid hydrates [*Koop et al.*, 1995; *Biermann et al.*, 1996; *Salcedo et al.*, 2001; *Tabazadeh et al.*, 2001] or special nuclei [*Tolbert and Toon*, 2001] have been proposed to explain the selective nucleation process. It has also been suggested that lee-wave clouds play a role in the formation of denitrifying NAT particles [*Carslaw et al.*, 1998; *Dhaniyala et al.*, 2002]. In situ measurements of large particles are critical in order to constrain the different nucleation processes.

[5] In the past, low number density populations of large HNO_3-containing particles in the Arctic or Antarctic may have eluded detection due to measurement and interpretation limitations. The few particle instruments that have sampled polar stratospheric air generally have limits of detection near 10^{-3} cm^{-3}. The meteorological conditions in some winters, especially in the Arctic, may have been such that large particles simply did not form. Some populations of large particles with low number densities have been measured in the polar stratospheres, particularly during the Arctic winter of 1989 [*Dye et al.*, 1990; *Wofsy et al.*, 1990; *Hofmann and Deshler*, 1991; *Goodman et al.*, 1997]. However, without simultaneous measurements of composition in most cases, these particles were assumed to be ice or NAT-covered ice. This led to the speculation that denitrification could occur as ice particles fell through NAT-saturated regions of the stratosphere and acquired a layer of NAT through condensation [*Wofsy et al.*, 1990]. Based on the results presented here, particles observed in these earlier studies may indeed have included large NAT particles.

[6] The observations presented here derive from the 1999/2000 joint Sage III Ozone Loss and Validation Experiment (SOLVE)/Third European Stratospheric Experiment on Ozone (THESEO 2000). Extensive measurements of large (>2 μm) HNO_3-containing particles were made during SOLVE/THESEO 2000 with three instruments on board the NASA ER-2 [*Fahey et al.*, 2001]. The formation and sedimentation rates of these large particles suggest a viable mechanism for the observed severe and widespread denitrification of the 1999/2000 Arctic winter [*Popp et al.*, 2001]. Extensive ozone loss was also observed during the SOLVE/THESEO 2000 campaign [*Sinnhuber et al.*, 2000; *Richard et al.*, 2001]. The combined measurements of large HNO_3-containing particles, widespread irreversible denitrification, and ozone loss during the SOLVE/THESEO 2000 campaign offer a unique opportunity to answer remaining questions about PSC nucleation and composition, denitrification, and the role of PSCs in chemical ozone loss [*Gao et al.*, 2001].

[7] A preliminary analysis of large particle observations in SOLVE/THESEO 2000 has been presented by *Fahey et al.*, [2001] using two NO_y ($NO_y = HNO_3 + NO + NO_2 + N_2O_5 + ClONO_2 + \ldots$) data intervals taken during the flight of 20 January in the polar vortex. Assuming NAT composition, this study estimated particle sizes up to 20 μm diameter. Although the total number concentration is low (near 10^{-4} cm^{-3}), the calculated instantaneous HNO_3 flux values associated with the largest particles are sufficient to cause appreciable denitrification of the lower stratosphere if sustained for a matter of days. An atmospheric model with microphysical processes was used to simulate the growth, sedimentation, and advection of NAT particles with sizes up to 20 μm. Growth times for 2–20 μm diameter NAT particles from nucleation were estimated to be from less than a day up to 6 days. In a further study, particle nucleation process were constrained by comparing results obtained using different nucleation mechanisms with large particle observations [*Carslaw et al.*, 2002]. Results indicate that synoptic-scale ice saturation conditions do not likely play a role in the highly selective nucleation process of large NAT or NAD particle formation.

[8] In this study the discussion of large HNO_3-containing particles is expanded to include all of the 1999/2000 Arctic winter data set. The primary objectives of this paper are (1) to describe the sampling and detection of large HNO_3-containing particles using an NO_y detector with two heated inlets; (2) to provide diagnostics for the analysis of large particle data; and (3) to characterize all the observations of large particles in the Arctic 1999/2000 winter stratosphere. A combination of

analytical methods is used to determine sizes and concentrations for the wide range of large particle populations that was observed during the SOLVE/THESEO 2000 mission. These methods are used to demonstrate that large particles with sizes up to 20 μm diameter were present on several days over a 48-day observation period, over large areas inside the vortex, and over a considerable range of altitudes. The observations will be discussed in the context of the vortex meteorological fields and areas of NAT saturation.

[9] The study begins in section 2 with a description of the NO_y instrument and its aerosol sampling characteristics. Section 3 presents the large particle observations taken with the NO_y instrument during the 1999/2000 Arctic winter. Section 4 presents a diagnostic for interpreting particle sizes and number densities from NO_y time series.

2. Instrumentation

[10] This study makes use of several measurements made on board the NASA ER-2 aircraft, including total NO_y, H_2O vapor, vertical temperature profile, and local temperature and pressure. Of principle interest to this study are the sampling and detection of gas-phase and aerosol NO_y, described in detail in sections 2.1 and 2.2. H_2O vapor was measured with the JPL Laser Hygrometer, a near-infrared tunable diode laser spectrometer [*May*, 1998]. A microwave temperature profiler (MTP) provided a passive measure of the temperature field approximately 4 km above and 3 km below the ER-2 aircraft [*Denning et al.*, 1989]. Local temperature and pressure along the flight track were measured using the ER-2 Meteorological Measurements System (MMS) [*Scott et al.*, 1990]. HNO_3 and H_2O profiles were used from remote high-latitude measurements obtained by the balloonborne MkIV interferometer during SOLVE/THESEO 2000 [*Toon*, 1991].

2.1. NO_y Detection

[11] NO_y and NO were measured using a three-channel chemiluminescence detector located in the lower fuselage payload area of the NASA ER-2 aircraft. Details of the instrument have been described previously [*Fahey et al.*, 1989; *Gao et al.*, 1997]. For the SOLVE/THESEO 2000 mission the instrument was modified from a previous configuration to include two independent channels for the detection of NO_y. The flow diagram of the modified instrument is depicted in Figure 1. In both the $F$$NO_y$ and $R$$NO_y$ channels, ambient gas-phase and particulate NO_y are sampled and reduced to NO through reaction with CO on a heated gold catalyst. Subsequently, NO reacts with O_3 in a chemiluminescent reaction to produce electronically excited nitrogen dioxide (NO_2) molecules. Some of the excited state NO_2 molecules decay to the ground state via emission of infrared photons, which are detected by a photomultiplier tube. In a third channel NO is sampled and detected by chemiluminescence. The mass flow for all three channels is controlled at 1 slpm (standard liter per minute). The instrument sampling rate is 1 Hz, which corresponds to 200 m of flight path.

2.2. Aerosol Sampling

[12] Both NO_y inlets are located in an external housing, the center of which is 48 cm below the fuselage of the ER-2. A schematic of the external inlet housing is shown in Figure 2. The two NO_y channels are designed to make identical independent measurements of NO_y when ambient NO_y has no aerosol component. In the presence of particles, the external inlet housing acts as a particle separator. The front, forward facing $F$$NO_y$ inlet samples gas-phase NO_y and particles of all sizes. The second inlet, the $R$$NO_y$ inlet, is also forward facing but is located at the rear of the external inlet housing. Because of the airflow streamlines around the particle separator, air entering the $R$$NO_y$ inlet is inertially stripped of particles above about 2 μm in diameter [*Fahey et al.*, 1989; S. Dhaniyala et al., manuscript in preparation, 2001]. Therefore, when the difference signal, ($F$$NO_y$ inlet signal - $R$$NO_y$ inlet signal), hereafter referred to as net NO_y, is greater than a few tenths of a ppbv, particles greater than 2 μm in diameter are being sampled by the $F$$NO_y$ inlet but not by the $R$$NO_y$ inlet.

[13] Upon entering one of the two NO_y inlets, an air sample is heated to 308 K by the walls of the inlet tubing. Particulate NO_y in the form of HNO_3 rapidly evaporates as the sample temperature increases above 200 K. At 50 hPa the sample residence time in an NO_y inlet upstream of the catalyst is approximately 4 ms. Calculations suggest that when heated to 308 K, a 20 μm diameter particle composed of 3:1 H_2O/HNO_3 binary solution evaporates in approximately 70 ms. Particle evaporation is further aided by impaction on the heated walls of the Teflon (TM) tubing and flow control valve (Figure 2). The internal bends in the inlet line and valve ensure that particles above a few μm in size will impact on the wall and evaporate. Further downstream, sampled air is heated to 573 K in the catalytic converter. If particles do not fully evaporate before the sample reaches the catalyst, calculations suggest evaporation will occur in less than 1 ms at this temperature. With evaporation aided by impaction, essentially all condensed HNO_3 is detected as NO_y in both channels. As discussed below, because of the interaction of HNO_3 with the internal components of the instrument upstream of the catalyst, the released HNO_3 from a large particle is spread over more than one 1-s sampling period.

[14] The sampling of both NO_y inlets is subisokinetic; that is, the flow velocity (U) inside the sample opening is less than the aircraft true air speed (U_0) of 200 m s^{-1}. U is set by the constant sample mass flow and pressure at the inlet opening. For subisokinetic conditions, particle number concentrations expressed as number per unit volume of air (number per cubic centimeter of air) inside the inlet are enhanced above ambient values. Similarly, particle concentrations expressed as number per unit mass of sampled air (number per gram of air) are enhanced above ambient values. The particle enhancement factor on a mass basis (EF_m) is related to the volumetric particle enhancement factor (EF_v) by the ratio of the ambient gas density (ρ_0) to the gas density in the inlet (ρ):

$$EF_m = EF_v \frac{\rho_0}{\rho}. \quad (1)$$

In order to account for the enhancement of NO_y mixing ratios, EF_m values are used in this study.

[15] The computational fluid dynamics (CFD) program FLUENT (Fluent, Inc., Lebanon, New Hampshire) was used to estimate enhancement factors by modeling the flow around the NO_y particle separator and calculating the trajectories of

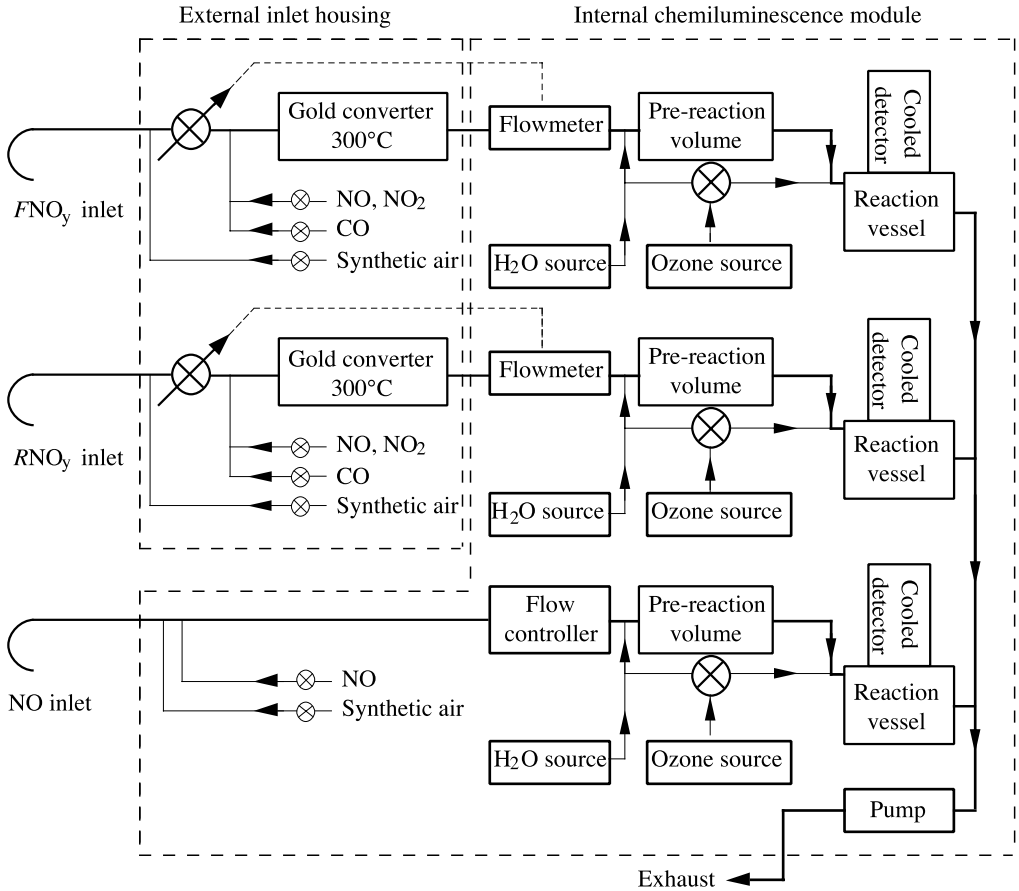

Figure 1. Flow diagram of the three-channel NO_y instrument used on the ER-2 aircraft showing both the external inlet housing and the internal NO/O_3 chemiluminescence module. NO_y is sampled from two points located on the external inlet housing (FNO_y and RNO_y inlets). NO is sampled from an inlet extending from the bottom of the aircraft fuselage. The internal chemiluminescence module is located in the lower fuselage payload area of the NASA ER-2, and the external inlet housing (shown in Figure 2) extends 48 cm from the bottom of the aircraft.

NAT spherical particles (density = 1.62 g cm^{-3}) of various sizes around the particle separator and near the inlet openings (S. Dhaniyala et al., manuscript in preparation, 2001). The model explicitly uses the two-dimensional axisymmetric shape of the particle separator body, so the modeling of the front inlet is reduced to a two-dimensional problem. The rear inlet, which is located 2 cm away from the surface of the separator, was modeled as a pipe opening in free stream to avoid detailed three-dimensional modeling at that location.

[16] The values of EF_m for the sampling of both inlets are shown as a function of particle size in Figure 3. A value of zero indicates that no particles are sampled at that size. At the largest sizes, EF_m for the front inlet approaches U_0/U. As the free stream pressure increases, EF_m for both inlets increases due to the change in U at constant mass flow. The "pipe" results for the rear inlet indicate similar enhancements to those estimated using the semiempirical expressions of *Fahey et al.* [1989] (S. Dhaniyala et al., manuscript in preparation, 2001). Calculated particle number concentrations at the rear inlet location are higher than those in the free stream because particle trajectories accumulate close to the particle separator surface as the particles pass around the front end of the separator body. This "accumulation effect" is evidenced by EF_m values for the RNO_y inlet signal which exceed those of a pipe opening in the free stream at sizes less than 2 μm diameter (Figure 3). Results for the front inlet enhancement are substantially lower than those for the pipe opening in the free stream due to the "blunt body" effect. This effect results from the presence of the particle separator body, which turns and slows the flow upstream of the FNO_y inlet, causing lower EF_m values for particles smaller than 10 μm. Due to the combination of the "accumulation" and "blunt body" effects, negative net NO_y values result when the RNO_y inlet samples a large number of particles with diameters less than 2 μm. Of particular importance to the present study are the large and relatively constant EF_m values above 10 μm diameter for the FNO_y inlet signal and the exclusion of particles larger than 2 μm diameter from the RNO_y inlet signal.

[17] For the sampling of the largest particles at 50 hPa in Figure 3 (100 μm diameter), EF_m is approximately 10. For this size, essentially all particles in the volume swept out by the inlet tubing inner diameter (0.40 cm) enter the inlet opening. For smaller particles EF_m decreases, indicating that not all particles in the swept volume enter the opening. During a single 1-s sampling period, both inlet openings

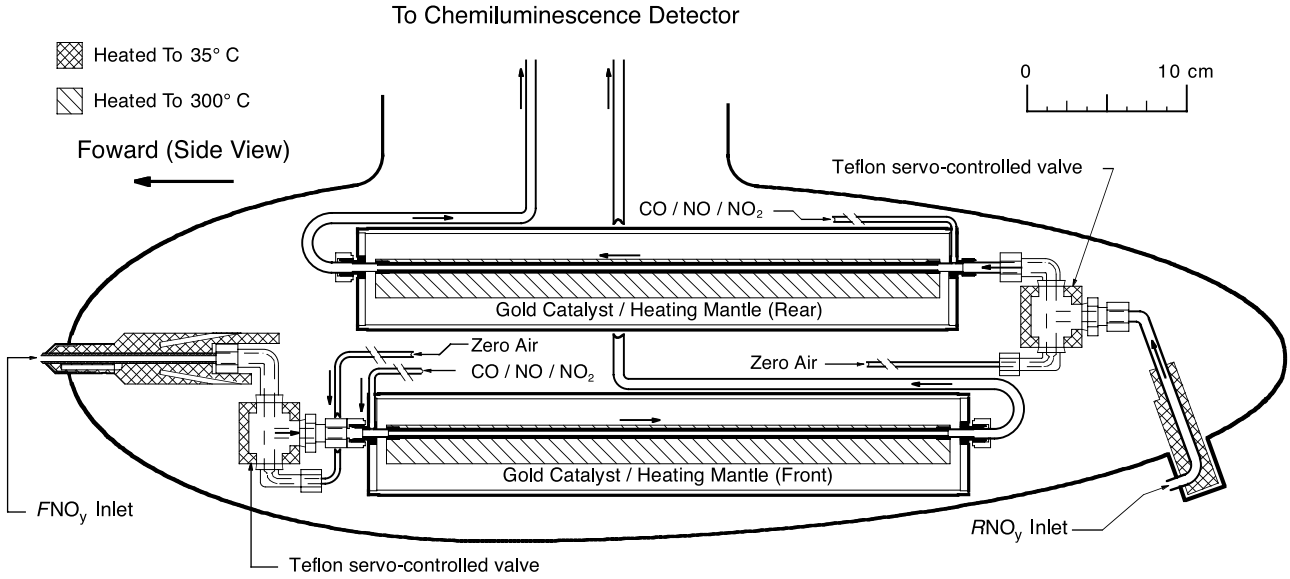

Figure 2. Cross-sectional view of the external inlet housing on the ER-2 aircraft showing both the front (FNO$_y$) and rear NO$_y$ (RNO$_y$) sampling points and internal components. When NO$_y$ has no aerosol component, the two inlets provide identical measurements of NO$_y$. The hatched areas denote thermostatted components. Particles greater than approximately 2 μm in diameter are inertially stripped from the RNO$_y$ measurement. Since HNO_3 tends to adsorb on surfaces, the gold converters are located as close to the sampling points as possible to minimize inlet line losses of the NO$_y$ species.

sweep through 2.5×10^3 cm^3. Hence, for the largest particle sizes, where EF_m is effectively U_0/U, a particle sampling frequency of 1 s^{-1} is equivalent to an ambient particle concentration of approximately 4×10^{-4} cm^{-3}.

[18] Isolated peaks occur in net NO$_y$ when particles with sizes greater than 2 μm are sampled at a rate less than 1 s^{-1} (Figure 4). A "tailing" effect or extended detection period is associated with the sampling of each particle. The extended detection period is attributed to the released HNO_3 adsorbing and desorbing to and from the Teflon walls of the inlet line upstream of the catalyst [*Neuman et al.*, 1999]. An examination of a large number of these single particle events shows that about 75% of a particle's total released HNO_3 is detected in the first second and the remainder is detected in the subsequent 20 seconds.

[19] Both NO$_y$ channels sample a constant mass flow of 1 slpm, regardless of ambient pressure and temperature. When a HNO_3-containing particle is sampled and evaporates in the NO$_y$ inlet, an absolute number of NO$_y$ molecules is subsequently detected. The net NO$_y$ volume mixing ratio (in ppbv) derived for the sampling of a single particle is the number of HNO_3 molecules released ratioed to the total number of molecules in the constant sample mass flow integrated over the 21-s "tailing" period. Thus the total net NO$_y$ released from a particle is independent of ambient temperature and pressure and can be expressed as the equivalent diameter (D_{NAT}) of a spherical NAT particle containing the same number of NO$_y$ molecules as:

$$D_{NAT} = 4.7\left(\text{net NO}_y\right)^{1/3}. \quad (2)$$

This expression accounts for the sample flow of the NO$_y$ instrument (1 slpm), the density of NAT (1.62 g cm^{-3}), and the molecular mass of NAT (117 g mol^{-1}). For NAD, with a density of 1.7 g cm^{-3}, the multiplicative factor in equation (2) becomes 4.4. The relationship between D_{NAT} and net NO$_y$ is plotted in Figure 5 for both NAT and NAD particle compositions. Recall that the computation of net NO$_y$ in

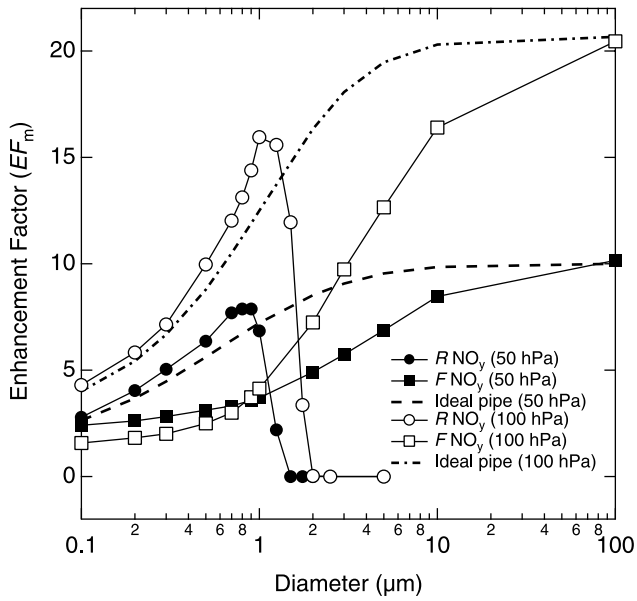

Figure 3. Modeled NO$_y$ instrument mixing ratio enhancement factors (EF_m) for the RNO$_y$ inlet signal (circles) and the FNO$_y$ inlet signal (squares) at 50 hPa (closed symbols) and 100 hPa (open symbols) compared to those for an ideal pipe (dashed lines) as a function of particle diameter. The CFD calculations were carried out assuming a particle density of 1.62 g cm^{-3}, mass flow rate of 1 slpm, aircraft speed of 0.7 Mach, and ambient temperature of 200 K (S. Dhaniyala et al manuscript, in preparation, 2001).

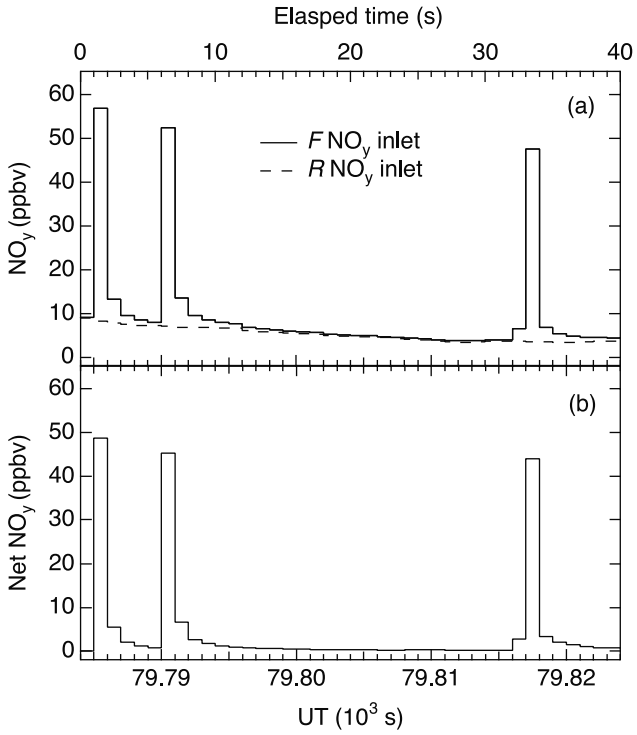

Figure 4. (a) NO_y mixing ratios from the $R$$NO_y$ (dashed line) and $F$$NO_y$ (solid line) inlets during a period when large particles are sampled by the $F$$NO_y$ inlet. (b) Net NO_y ($F$$NO_y$ inlet signal - $R$$NO_y$ inlet signal) mixing ratios. Using equation (2), NAT particle diameters for these three particles are approximately 18–19 μm. Up to 75% of the total HNO_3 released from a particle is detected in the first second. The remaining HNO_3 is detected in the subsequent 20 s.

equation (2) involves the subtraction of the $R$$NO_y$ inlet signal which may be enhanced by the sampling of particles smaller than 2 μm (Figure 3). In this study enhancement effects in the $R$$NO_y$ inlet signal are neglected in equation (2) because the small (<2 μm diameter) particle mass is generally much less than the large (>2 μm diameter) particle mass.

[20] Because the HNO_3 released from a particle is detected over many seconds, the total amount of HNO_3 released from the particle should be used as the "net NO_y" value in equation (2). For example, for the second particle peak in Figure 4b, 45.3 ppbv of net NO_y was detected during the first second, 6.7 ppbv during the second, 2.7 ppbv during the third second, etc., for a net NO_y total of 65.0 ppbv. Net NO_y integrated over the entire 21-s time period yields a particle size of 19.0 μm diameter from equation (2), whereas using the peak value of net NO_y, (45.3 ppbv), results in an underestimated diameter of 16.8 μm. Generally, integration for each particle peak over the 21-s period is not possible because high particle concentrations cause the time between particle sampling events to be less than 20 s. Furthermore, at very high particle concentrations, more than one particle may be sampled during a 1-s sampling period. Therefore 1-s net NO_y values are not a direct indication of particle size. The net NO_y value, also referred to as the large particle signal, increases with the number or size of particles sampled. Section 4 addresses the issues of multiple particle sampling and the distribution of particle HNO_3 over several sampling intervals. By careful treatment of both of these problems, it is sometimes possible to convert net NO_y values from the time series to particle sizes and concentrations.

[21] The peaks in Figure 4 are assumed to be due to the sampling of individual large HNO_3-containing particles. It is not likely that an individual peak is due to the sampling of more than one smaller particle. For example, it is assumed that the particle signal for the second peak in Figure 4 is due to the sampling of one 19-μm particle at 79 790 UT followed by no other particles for over 20 seconds, instead of a "packet" of several hundred 2-μm particles arriving at the detector simultaneously at 79 790 UT, followed by no particles for over 20 seconds. Apart from the lack of a physical atmospheric process that supports this idea of particle "packets," the "single particle" assertion is justified by two key facts. First, particle measurements taken by the Multiangle Aerosol Spectrometer Probe (MASP) instrument on board the ER-2 indicate low number density populations of large particles present along the discussed flight tracks [*Fahey et al.*, 2001]. Second, because 2-μm particles evaporate quickly at temperatures above T_{NAT}, they would only be observed routinely at temperatures below T_{NAT}, contrary to the results presented below.

3. Observations

3.1. Flight Summary

[22] The data used in this analysis were collected during two phases of the SOLVE/THESEO 2000 mission: 20 January to 3 February 2000 and 26 February to 16 March 2000. Hereafter, the two periods will be referred to as the midwinter and late winter sampling periods, respectively. During these two periods, large PSC particles were detected by the NO_y instrument during seven ER-2 flights in the Arctic vortex. The vortex was well sampled in equivalent latitude for both of these periods (P. Newman, personal

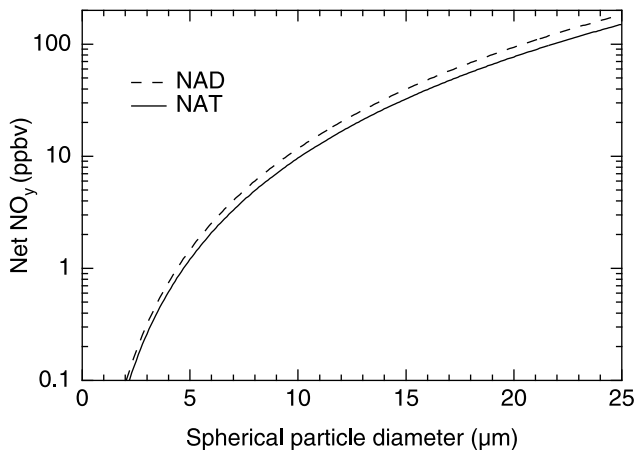

Figure 5. Net NO_y as a function of spherical NAT (solid line) and NAD (dashed line) particle diameter calculated using equation (2). Here, net NO_y is the total amount of HNO_3 released from a particle, since the HNO_3 is detected over many seconds (see section 2.2).

communication, 2000). Large particles were observed on the first ER-2 flight in the Arctic vortex, 20 January, and on every subsequent flight until 7 March. In addition to these seven flights, large particles were encountered on the ER-2 flights of 23 January and 2 February. However, instrument problems prevented adequate quantification of net NO_y on these days; hence these flights are not included in the discussion. Large particles were not observed during the three SOLVE/THESEO 2000 flights after 7 March, on 11, 12, and 16 March. Figure 6 illustrates the ground flight tracks for the seven large particle flights indicating with heavy yellow lines the approximate locations of large particles. For each flight, the temperatures and vortex edge at the primary ER-2 flight level are indicated. Here large particle locations are noted as segments of the flight track where peaks greater than 1 ppbv (5 μm diameter) were regularly observed in net NO_y. With the exception of the flight of 27 January, all flights shown were conducted entirely inside the Arctic vortex. All flight tracks begin and end at the deployment site, Kiruna, Sweden, (68 °N). For most flights, the ER-2 flew at cruise altitudes near 19–20 km (420–450 K), with at least one vertical profile made during each flight to reach near 16 km.

3.2. Geographical Distribution of Large Particles

[23] During the midwinter period large particles were a widespread phenomenon of the Arctic vortex, as demonstrated by the thick yellow lines in Figure 6. Particles were observed between 60 °N and 85 °N over thousands of kilometers of the vortex during these four flights. As shown by the temperature fields in Figure 6, for most observations temperatures were less than 198 K and hence near or below NAT saturation temperatures (T_{NAT}) at cruise altitudes. From meteorological analyses of this period, the vortex was unusually cold with large areas of the vortex below T_{NAT} near the 50 hPa level (~20 km) [*Manney and Sabutis*, 2000].

[24] The thin yellow lines in Figure 6 indicate flight track segments during which large particles were not observed during the SOLVE/THESEO 2000 mission. On 27 January 2000, the ER-2 flew outside of the polar vortex and into a warm pool over Russia with temperatures up to 212 K. On this day particles were only observed on the edge of the vortex at approximately 60 °N. Outside the vortex, temperatures were too high for the persistence of large NAT or NAD particles. However, large particles were not observed inside the vortex on this day either. In addition, on 20 and 31 January large particles were absent near Kiruna at the edge of the vortex. During the late winter period, large particles were absent over large segments of the ER-2 flights (Figure 6). Temperatures at ER-2 flight levels during this period were generally comparable to the midwinter phase or slightly higher. Minimum temperatures near the 50 hPa level were higher than they were during the midwinter sampling period but remained below T_{NAT} throughout both periods [*Manney and Sabutis*, 2000].

[25] Time series of net NO_y, ambient temperature, and altitude are shown in Figure 7 for the seven SOLVE/THESEO 2000 ER-2 flights in Figure 6. Net NO_y values exceeded 100 ppbv on 20 and 31 January and 3 February. During these three flights, a large particle was encountered on average once every two seconds. The most extensive population of large particles was measured on 20 January. The greatest large-particle signal of the mission of 260 ppbv, was measured on 31 January. During the late winter period, large particle measurements were more sporadic, less frequent, and much less intense (net $NO_y < 20$ ppbv) as compared to the midwinter period (Figure 7). For example, on 7 March, a particle was sampled by the NO_y instrument only every few hundred seconds or so, corresponding to number concentrations much less than 10^{-5} cm^{-3}.

[26] Note that the reported net NO_y mixing ratios are not the equivalent gas-phase NO_y incorporated in large particles. To calculate equivalent gas-phase mixing ratios, average net NO_y values must be adjusted to account for the EF_m values of sampled particles (Figure 3). The size distribution of a particle population must be known in order to determine this value accurately. Also note that negative net NO_y values occur a number of times in Figure 7. The negative net NO_y values arise because of differences between the RNO_y and FNO_y inlets in the sampling of small particles (<2 μm diameter, see section 2.2) and occur primarily when numerous small particles are present in the absence of a significant number of large particles. The FNO_y inlet signal values in these instances are generally small (less than a few ppbv).

3.3. Vertical Distribution of Large Particles

[27] Net NO_y versus altitude is shown in Figure 8 for all seven of the ER-2 flights during which large particles were detected. Note that unlike Figure 7, the net NO_y values in Figure 8 are shown on the same scale so that the relative net NO_y values for the different flights may be compared. Large particles were observed at all altitudes between 15 and 21 km. The ER-2 does not reach altitudes greater than 21 km, and altitudes less than 15 km are only reached during ascent and descent. On 20 January during the mid-flight vertical profile (Figure 7) the large-particle signal was significant at all altitudes between 16 and 20 km. However, on 31 January and 3 February large-particle signals were higher at 15–16 km than at ER-2 cruise levels. This is particularly evident during the multilevel flight of 3 February. On this day, the ER-2 flew extended flight legs through PSCs at 4 different altitudes (see Figure 7). Two of these altitudes are clearly distinguishable at 15.7 km and at 17.2 km in Figure 8, where large-particle signals were highest at the 15.7 km flight level. At this pressure altitude, particles were likely in the "subvortex" region (<400 K potential temperature level; see *McIntyre* [1995]). During the late winter period, large-particle signals were much less intense and particles were not detected below 17.5 km.

[28] A strong contrast between the midwinter and late winter periods is shown by Figures 6, 7, and 8. Large particles formed during both sampling periods, yet to a very different extent. During the midwinter period large particles were more widespread and large-particle signals were generally much higher than during the late winter period. However, the temperature fields inside the vortex at ER-2 cruise altitudes for each of the seven flights appear similar to one another (Figure 6). On the first and last flight date, flight level temperatures in the vortex from meteorological and aircraft observations were 198 K or less. This result highlights the fact that local temperatures along the flight tracks cannot be used to predict accurately the existence or absence of large HNO_3-containing particles nor the differ-

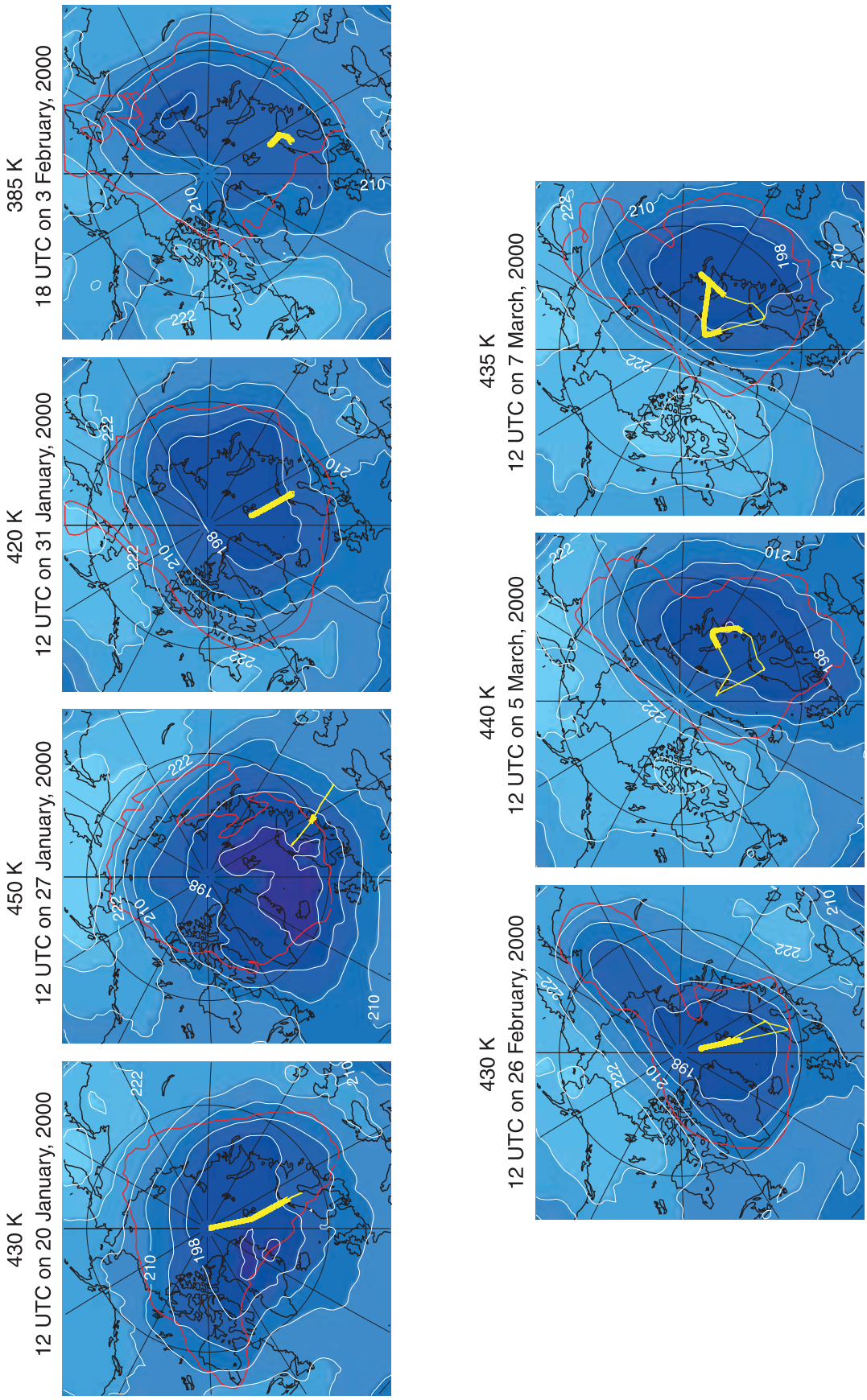

Figure 6. Maps of the NASA ER-2 ground tracks (yellow lines) for all flights during which large particles were observed. The heavy portions of the yellow lines indicate where large particles were observed. Also shown are temperatures (white contours and color shading) on an isentropic surface (labeled) that is representative of the flight. The vortex edge on this surface is marked in red. The meteorological results are from the NCEP analyses for the flight date and indicated time.

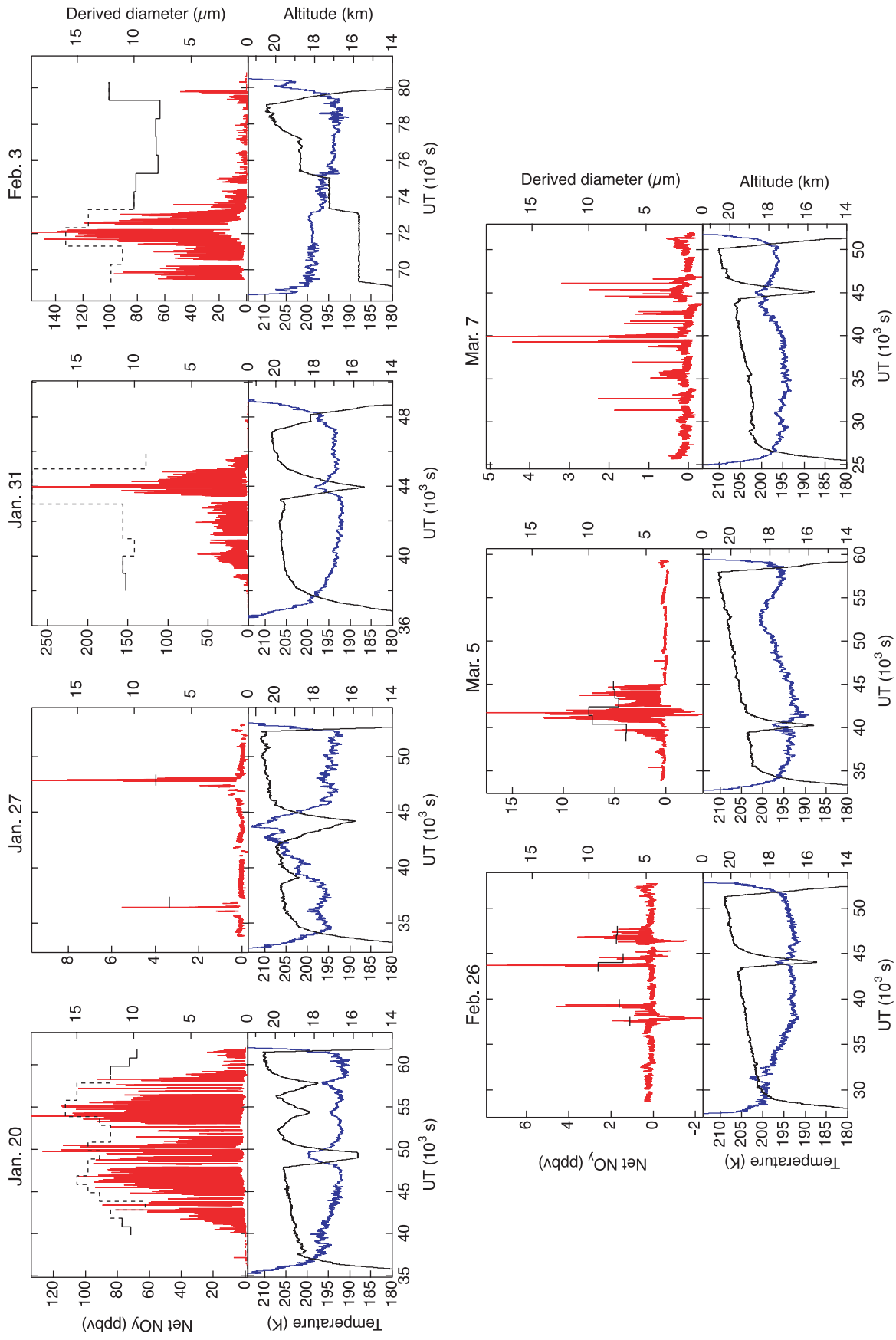

Figure 7. Net NO_y (red lines, top left), derived mean particle size (black lines, top right), temperature (blue lines, bottom left), and altitude (black lines, bottom right) versus universal time (UT) in seconds for the seven flights during which large particles were sampled. The single particle detection method (solid black line) was used to derive NAT particle diameters when total number concentrations were less than 10^{-4} cm^{-3}. The probability method (dashed black line) was used for particle concentrations greater than 10^{-4} cm^{-3}. Note that the net NO_y scale is different for each plot.

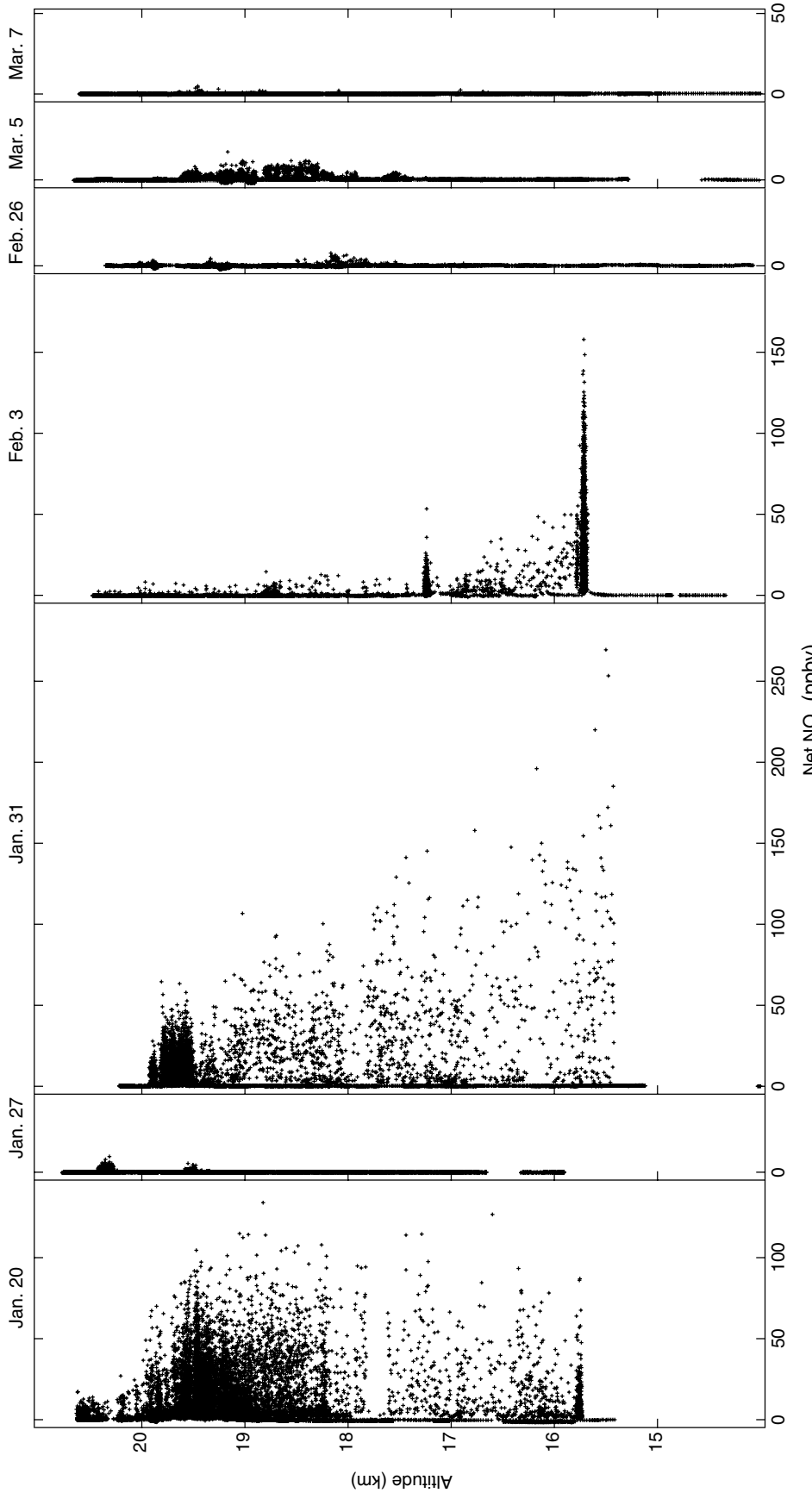

Figure 8. Vertical distribution of net NO_y values for the seven flights during which large particles were detected. The dates designate flights in the 1999/2000 winter. The horizontal scale is the same for each flight. The data are 1-s average values.

ences in the intensity of large-particle signals. The large particles were not in equilibrium with the air from which they were sampled; hence equilibrium models cannot be used to calculate the amount of condensed phase HNO_3 in an air parcel.

3.4. Particle Composition

[29] The large particles discussed in this study are assumed to be composed of NAT, because it is the stable hydrate of the HNO_3/H_2O system at winter polar stratospheric conditions [*Hanson and Mauersberger*, 1988]. Alternatively, particles could be composed of NAD, a metastable phase at these conditions. According to laboratory studies, NAD has a lower nucleation barrier and higher HNO_3 vapor pressure than NAT [*Worsnop et al.*, 1993]. It is unlikely that large particles are composed of STS, since STS particles must be in equilibrium with available HNO_3 and H_2O [*Carslaw et al.*, 1995]. Calculations show that at the observed conditions there is too little HNO_3 and H_2O in the liquid STS phase to account for the estimated average amounts of condensed HNO_3 along the flight track. For simplicity, quantitative analyses are carried out here assuming NAT composition. It is also assumed that all of the measured net NO_y is HNO_3 and that no other NO_y species are present in the particles.

3.5. NAT Saturation

[30] The saturation mixing ratio of HNO_3 over NAT, ($[HNO_3]_{sat}$), was calculated from ambient measurements of H_2O vapor, temperature, and pressure using the expressions derived in the laboratory study of *Hanson and Mauersberger* [1988]. The uncertainty in this empirical formula is ± 30%. The NAT saturation ratio, (S_{NAT}), is defined as the ratio of the ambient gas-phase HNO_3 to $[HNO_3]_{sat}$, where an S_{NAT} value of 1 represents equilibrium. If $S_{NAT} > 1$, the air is supersaturated with respect to NAT. Conversely, if $S_{NAT} < 1$, the air is subsaturated with respect to NAT. For simplicity this study excludes gas-phase removal of HNO_3 by other condensed phases such as STS. When present in an air parcel, STS particles limit the amount of available gas-phase HNO_3 for NAT particle growth and decrease S_{NAT} values, especially at temperatures below about 192 K [*Del Negro et al.*, 1997]. Estimating actual S_{NAT} values requires detailed knowledge of the phase and size distribution of small PSC particles and hence is beyond the scope of this study.

3.5.1. NAT saturation along the ER-2 flight tracks

[31] In this section, measurements of H_2O vapor, temperature, and pressure along the flight track were used to calculate $[HNO_3]_{sat}$. To calculate S_{NAT} values, ambient gas-phase HNO_3 was approximated by the RNO_y inlet signal with the implicit assumption that non-HNO_3 NO_y species are a small fraction of NO_y. The low NO/NO_y ratios observed throughout the vortex during SOLVE/THESEO 2000 support this assumption. Hence S_{NAT} is approximated as $[RNO_y]/[HNO_3]_{sat}$. When $S_{NAT} > 1$, small PSC particles may also be present along the flight track and enhance the RNO_y inlet signal significantly (see Figure 3) above ambient levels of gas-phase HNO_3 [*Del Negro et al.*, 1997]. In this case, the RNO_y value serves as an upper limit to gas-phase HNO_3, and hence the associated S_{NAT} values are also upper limits. S_{NAT} is plotted versus net NO_y in Figure 9 for the seven SOLVE/THESEO 2000 flights where large particles were observed. Data points with $S_{NAT} < 1$ and net $NO_y > 1$ represent measurements of large particles in air subsaturated with respect to NAT. Assuming these particles are NAT, they must have been evaporating when sampled. Conversely, data points with $S_{NAT} > 1$ and net $NO_y > 1$ represent measurements of large particles in air supersaturated with respect to NAT. Hence these NAT particles are accumulating HNO_3 and growing in size. As expected, most large particle measurements were obtained at apparent S_{NAT} values between 1 and 100, consistent with conditions under which NAT particles are stable or growing. In several cases, however, there are substantial large-particle signals at $S_{NAT} < 1$. Because S_{NAT} is an upper limit, these subsaturated air parcels are a subset of all such parcels. The color altitude scale demonstrates that many of the evaporating particles were found below typical ER-2 cruise altitudes (Figure 9), particularly during the flights of 20 January and 3 February. The observation of large particles in air subsaturated with respect to NAT provides evidence that the observed peaks in net NO_y are due to single large particles and not "packets" of many smaller particles. Packets of smaller particles would evaporate rapidly when $S_{NAT} < 1$ and hence would not be routinely observed.

3.5.2. NAT saturation above and below the ER-2 flight tracks

[32] The large NAT particles that cause the net NO_y values in Figure 8 have sizes up to approximately 20 μm diameter based on the diagnostics presented in section 4.0. Such large particles take days to grow to the observed sizes and reach sedimentation speeds up to 2 km day^{-1} [*Fahey et al.*, 2001; *Carslaw et al.*, 2002]. Therefore a key factor in the discussion of large particles is the S_{NAT} profiles above and below the ER-2 flight tracks. The S_{NAT} profiles were estimated using the remote temperature profile measurements made from the ER-2 and assumed profiles of HNO_3 and H_2O [*Hanson and Mauersberger*, 1988]. Single vertical profiles for HNO_3 and H_2O were used for all flights. The profiles were obtained on the 15 March 2000 flight of the MkIV Interferometer from the balloon facility at Esrange (68 °N), near Kiruna, Sweden [*Toon*, 1991]. Values for 1-km altitude intervals are listed in Table 1. For each recorded temperature, HNO_3 and H_2O values were interpolated to the corresponding altitude to calculate S_{NAT}. The resulting distribution of S_{NAT} values is shown in Figure 10 for the seven flights shown in Figure 8.

[33] Because a single profile is used for HNO_3 throughout, the results shown in Figure 10 only serve as a guide to the location of subsaturated and supersaturated NAT regions. The NO_y reference state values (NO_y^*) in Table 1 indicate significant denitrification above 19 km. Based on ER-2 observations, inner vortex air parcels were denitrified up to 70% [*Popp et al.*, 2001]. Note that the color scale in Figure 10 is logarithmic; thus a factor of 2 change in the HNO_3 profile results in a change in Figure 10 nearly undetectable by visual inspection. Thus the choice to use a single HNO_3 profile for all seven of the flights is reasonable in this case. Moreover, the conditions above the flight tracks in Figure 10 are not necessarily representative of those experienced by the sampled particles because of meteorological changes and particle advection. However, Figure 10 demonstrates that cold pools, and hence areas of

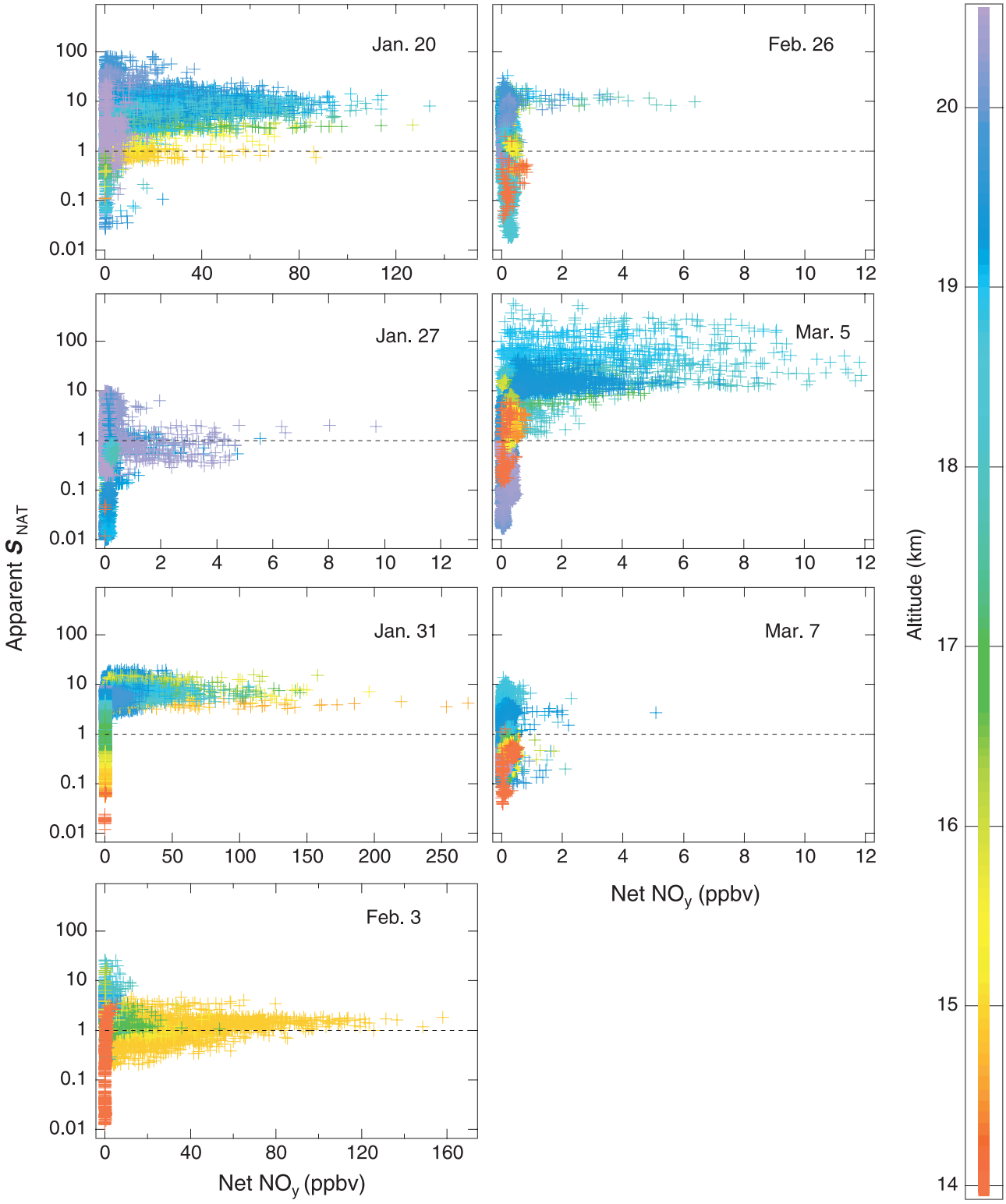

Figure 9. Apparent S_{NAT} (defined as $[RNO_y]/[HNO_3]_{sat}$) versus net NO_y for the seven flights where large particles were observed. The data are colored as a function of altitude at which each 1-s observation was made. In each graph, the dashed line marks $S_{NAT} = 1$. Data points below this line with net $NO_y > 1$ represent large particles in air subsaturated with respect to NAT. Data points above this line with net $NO_y > 1$ represent measurements of large particles in air supersaturated with respect to NAT. Apparent S_{NAT} values are upper limits under some conditions (see section 3.5.1).

Table 1. Data from the MkIV flight of 15 March from Esrange (68 °N), near Kiruna, Sweden used in the calculation of NAT saturation conditions (Figure 10)

Altitude (km)	HNO_3 (ppbv)	H_2O (ppmv)	NO_y^* (ppbv)
14	3.7	4.4	3.4
15	4.2	4.4	3.1
16	5.2	4.6	3.3
17	6.0	4.9	4.7
18	5.9	5.3	6.9
19	5.9	5.7	9.4
20	7.1	6.1	12.2
21	8.4	6.6	14.6
22	8.1	7.0	16.1
23	6.7	7.0	17.1
24	4.9	6.9	17.1

NO_y* values were calculated using measured N_2O according to the reference state established by *Popp et al.* [2001].

NAT saturation were large-scale features of the 1999/2000 Arctic vortex.

[34] For all flights shown in Figure 10, most large particles were sampled in or directly below areas of the stratosphere with $S_{NAT} > 1$. The notable exceptions are the few particles sampled in the vertical profile on 7 March. The most widespread region of S_{NAT} between 10 and 100 occurred above the flight track on 20 January, coinciding with the most widespread population of large particles sampled by the NO_y instrument during the SOLVE/THESEO 2000 mission (Figure 6). Large particles were not observed in areas of the atmosphere that were highly subsaturated ($S_{NAT} < 0.1$) with respect to NAT, for example on 27 January (40 000–47 000 UT), and 5 March (49 000–55 000 UT). Large particles were observed in slightly subsaturated areas of the vortex ($0.1 > S_{NAT} < 1$). These sampling points typically were directly below highly saturated regions of the atmosphere below ER-2 cruise altitudes, for example, on 20 January (49 000 UT) and 3 February (70 000–74 000 UT). For both of these sampling intervals ambient temperatures were near 200 K and pressures were near 100 hPa. Large NAT particles could remain at these conditions for one or more days before complete evaporation. Lastly, the areas of NAT saturation were smaller during the late winter period of SOLVE/THESEO 2000 as compared to the midwinter period. Correspondingly, large particle observations were less frequent, (as shown by the broken heavy line in Figure 10, 7 March), and measured large-particle signals were less intense (Figure 8). Both features are consistent with smaller vortex regions of NAT saturation conditions.

[35] According to U.S. National Center for Environmental Prediction (NCEP) data, vortex minimum temperatures at the 30, 50, and 70 hPa levels during the winter are consistent with the NAT saturation analysis presented in Figure 10. During the midwinter period, minimum temperatures at the 30 hPa level (~24 km) were unusually low, remaining below 190 K until the end of January (P. Newman, personal communication, 2000). The large areas of the polar vortex with temperatures below T_{NAT} are also presented by *Carslaw et al.*, [2002, Figure 2], where temperature fields are from the U.K. Met Office (UKMO) analysis. By the late winter period, however, minimum temperatures at the 30 hPa level had increased and remained above the nominal threshold for NAT particle formation used in the NCEP analysis. The absence of NAT saturation conditions at these pressure altitudes precluded particle nucleation and growth. Likewise, *Carslaw et al.* [2002, Figure 2] shows no areas of NAT saturation above about the 520 K potential temperature level. At the 50 and 70 hPa levels (~20, 18.5 km, respectively), however, parts of the vortex remained below T_{NAT} into late March. In these places particles may have nucleated and grown for short times, thus suggesting a possible explanation for the sporadic and low large-particle signals measured during the late winter sampling period.

3.6. Ice Saturation

[36] Ice particles have long been thought to play a role in the mechanism of denitrification [*Wofsy et al.*, 1990; *Toon et al.*, 1990; *Waibel et al.*, 1999]. For example, NAT could nucleate and accumulate on ice particles as they sediment through air that is supersaturated with respect to NAT. Laboratory evidence supports the possible role of ice in the heterogeneous nucleation of NAT [*Middlebrook et al.*, 1996]. However, this mechanism requires the pervasive existence of temperatures below the frost point, T_{ICE}, at altitudes well above sampling altitudes. A comparison of vortex temperatures and net NO_y observations taken during the 1999/2000 Arctic winter constrains the possible contribution of ice to the nucleation mechanisms of the large NAT particles. As shown in Figure 8, large particles continued to form into early March. However, according to NCEP data, vortex-wide minimum temperatures only fell below T_{ICE} one time at the 70 hPa level and not at all at the 50 or 30 hPa levels during the late winter period, assuming 4 ppmv of available H_2O vapor (P. Newman, personal communication, 2000). Also, the ice saturation ratio, S_{ICE}, along and above the ER-2 flight tracks was calculated using the MTP data in a similar manner to the S_{NAT} calculation described in section 3.5.2 using the *Smithsonian Institution* [1958] tables. Consistent with the NCEP data, results indicate that a very small fraction of the air parcels up to 4 km above the ER-2 flight tracks experienced temperatures below T_{ICE}. In addition, only very small areas of the polar vortex are found to be below the frost point as calculated using UKMO temperatures for the two SOLVE/THESEO 2000 sampling periods [*Carslaw et al.*, 2002, Figure 3]. Although the different meteorological data sets show that vortex temperatures below T_{ICE} did not occur frequently during either of the two ER-2 sampling periods, temperatures likely went below the ice frost point on some occasions in late December 1999 and early January 2000 [*Herman et al.*, 2002]. Although the role of mountain waves in particle nucleation cannot presently be ruled out [*Dhaniyala et al.*, 2002], it is unlikely that synoptic-scale ice saturation conditions played a major role in the nucleation and growth of the widespread large-particle populations shown in Figures 6 and 7.

4. Determination of Particle Sizes and Number Concentrations

4.1. Methodology

[37] In this section the conversion of intervals from the net NO_y time series to NAT or NAD particle size distributions is addressed. All three of the size determination

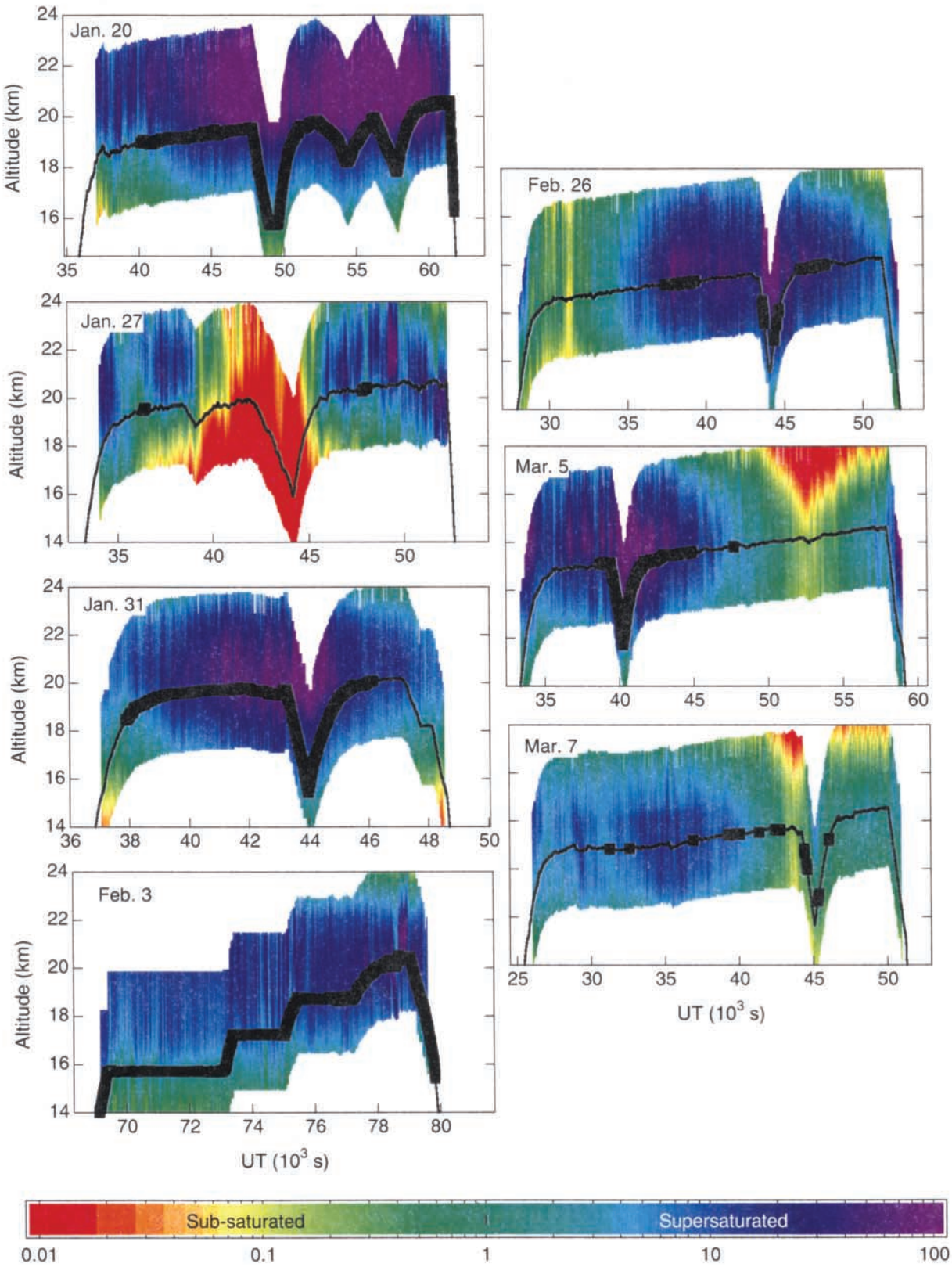

Figure 10. Vertical profiles of S_{NAT} versus UT for the seven flights during which large particles were sampled. The black line represents the ER-2 altitude flight track along which regions of large particle observations are indicated by the heavy portions of the line. S_{NAT} values are calculated from remote temperature profiles from the ER-2 and assumed HNO_3 and H_2O profiles.

methods discussed below rely fundamentally on the assumption that the sampled particles were randomly distributed within sampling intervals. Ideally, in determining a representative size distribution, the frequency and magnitude of peaks in the net NO_y time series would be uniform over periods of 500 to 1000 s or more. For most of the SOLVE/THESEO 2000 NO_y data set, this is not the case. Other limiting issues in the conversion process are multiple particle sampling and the spreading of HNO_3 from a particle over several seconds discussed in section 2.2. When more than one particle is sampled in a 1-s NO_y recording period, individual size information is lost. The spreading of HNO_3 causes a single particle to contribute to net NO_y in more than one sampling period. The parameters used in determining sizes and number concentrations of large particles from a net NO_y time series interval are the average net NO_y, the standard deviation of net NO_y, and the peak occurrence frequency. Peak occurrence frequency is defined as the number of peaks in a net NO_y times series interval divided by the interval width. Since the sampling period of the instrument is 1 Hz, the maximum peak occurrence frequency cannot exceed 1 s^{-1}. When the instrument is sampling less than one particle per second, peak occurrence frequency is proportional to particle concentration times the sweep volume. The exact relation between peak frequency and ambient concentration depends on the number of particles actually sampled during a 1-s period and the enhancement factors in Figure 3.

[38] Increases in ambient particle concentration increase the likelihood of multiple particle sampling during a sampling interval. If the spatial distribution of ambient particles is random within a flight track interval, then the probability, P, of counting n particles during a 1-s sampling period as a function of mean particle concentration is:

$$P(n) = \frac{\mu^n \exp(-\mu)}{n!}, \tag{3}$$

where μ is the mean number of particles sampled during the 1-s interval adapted from *Bevington and Robinson* [1992]. The value of μ is given by:

$$\mu = \frac{X}{E'} \frac{dV}{dt} t, \tag{4}$$

where x is the ambient particle concentration, t is the sampling period of the instrument, and E' is a correction term based on the enhancement factor. The term E' ranges from 1.6 to 1 for particle sizes of 5 to100 μm diameter respectively (Figure 3). The term dV/dt is the rate that volume is swept out by the inlet opening. The probability of sampling multiple particles in a single 1-s sampling period as a function of particle concentration is illustrated in Figure 11. For example, during one second of flight time, if the NO_y instrument is sampling a large-particle population with a total number concentration of 10^{-4} cm^{-3} (E' = 1), the probability is 80% that no particles will be sampled, and 18% that one particle will be sampled. For total particle concentrations of less than 6.2×10^{-5} cm^{-3}, the probability is less than 1% that more than one large particle will be sampled during a 1-s period. For this concentration, one particle will be sampled every 7 s on average, corresponding to a peak occurrence frequency of 0.15 s^{-1}. Thus this

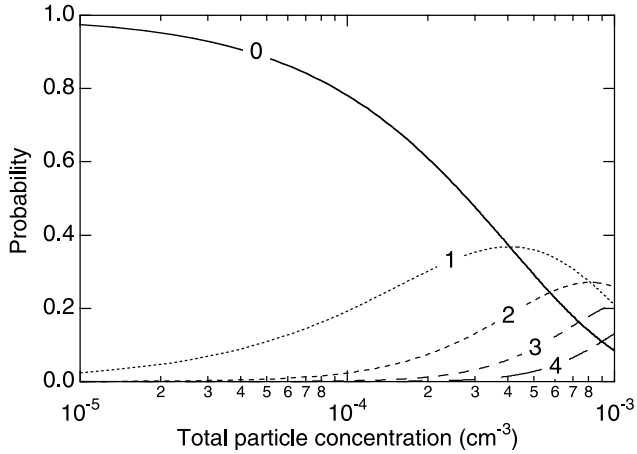

Figure 11. Probability of sampling 0, 1, 2, 3, or 4 (as labeled) randomly distributed particles during a 1-s net NO_y sampling period versus ambient particle concentration. Calculations were carried out using equations (3) and (4) with a true air speed of 200 m s^{-1}, inlet inner diameter of 0.4 cm, and net NO_y mass flow of 1 slpm.

frequency is chosen as a threshold for selecting the method of particle size determination. If the peak occurrence frequency exceeds this value, only a lower limit for particle concentration can be derived directly from the number of peaks in the time series. When the peak occurrence frequency in a data interval is less than 0.15 s^{-1}, particle peaks are interpreted as single particles (Single particle detection method, section 4.2).

[39] For data intervals with peak occurrence frequencies greater than 0.15 s^{-1}, less direct methods than the single particle detection method must be used to determine particle sizes. For those intervals in which the average and standard deviation of net NO_y are relatively constant for at least 500 to 1000 seconds, a numerical simulation can be used to determine particle sizes and concentrations (section 4.3). When the average and standard deviation of net NO_y are rapidly changing, a probability-based method is used to derive the most likely particle size for the interval (section 4.4). These three analytical methods for particle size retrieval are described below in detail.

4.2. Single Particle Detection Method

[40] The single particle detection method is used when the peak occurrence frequency is less than 0.15 s^{-1}. In this case, individual peaks can be discerned in the net NO_y time series (Figure 12a). At a peak frequency of 0.15 s^{-1}, on average a peak will occur in the net NO_y time series every 7 s. As described in section 2.2, the equivalent spherical diameter of an NAT particle can be calculated as a function of the total volume of HNO_3 released from a particle over the 21-s "tailing" period (equation (2)). Thus, in general, the area of a peak in the time series cannot be integrated over the entire 21-s "tailing" period before another peak occurs. In the single particle detection method, peak heights are used to approximate peak areas for the sampled particles.

[41] In order to make the peak area approximation, a decay function, R(t), was determined empirically to describe the sampling of an HNO_3-containing particle by

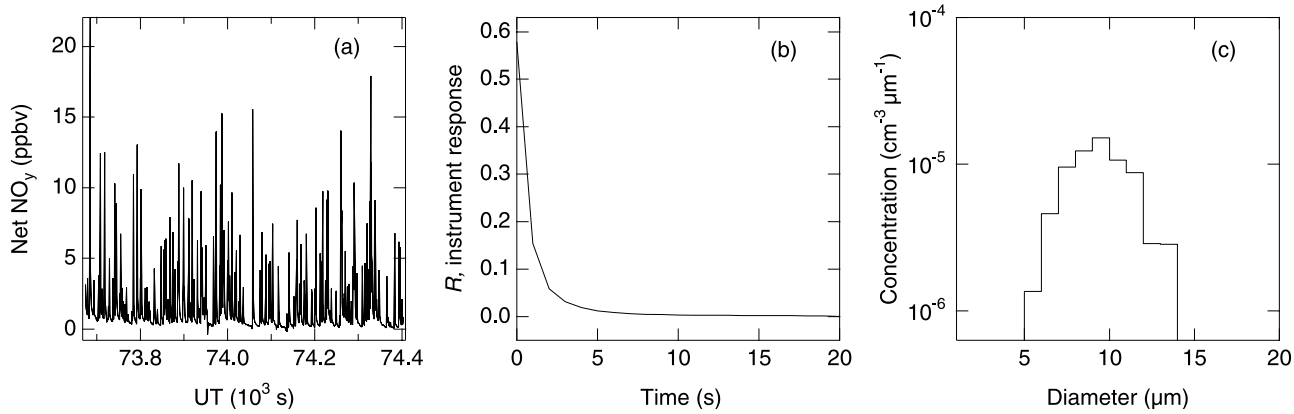

Figure 12. Single particle detection method applied to an interval from the flight of 3 February 2000. (a) Time series of approximately 800 s used in the analysis (73 647–74 403 UT). The data are 1-s average values. (b) Average modeled instrument response to HNO_3, $\bar{R}(t)$. (c) Resulting size distribution expressed as volume density.

the NO_y instrument. R(t) was derived by examining the time dependent signal from several individually resolved particles and determining a Lorentzian fit to the average of the normalized group. In general, the height and width of a particle peak depend on when the particle is sampled with respect to the start of each 1-s integration period in the detector. For example, given two particles of the same size (A and B), if particle A arrives early in the 1-s sampling period and particle B arrives late in the period, the first recorded net NO_y value that includes NO_y from particle A will be much larger than that for particle B. Conversely, the value of net NO_y in subsequent sampling periods will be higher for particle B than for A. Considering all possible particle arrival times within a 1-s interval yields the result that an average of approximately 60% of the HNO_3 released from a particle is recorded in the first sampling period and the remainder of the HNO_3 is detected over the next 20 s. The average function, $\bar{R}(t)$, is defined in Figure 12b, which shows the average distribution of detected HNO_3 from a particle over the 20 s interval after a particle is sampled.

[42] The complete expression for the conversion of a peak value of net NO_y (ppbv) to an NAT particle diameter (D_{NAT}) in μm is a modification of equation (2):

$$D_{NAT} = 4.7\left[\frac{\text{Net NO}_y(t_0) - \text{Net NO}_y'}{\bar{R}(0)}\right]^{1/3}, \qquad (5)$$

where net $NO_y(t_0)$ indicates the net NO_y peak value in ppbv recorded for the first second, t_0, of detection. As in equation (2), the multiplicative factor in equation (5) is 4.4 for NAD particles. The value $\bar{R}(0)$ is equal to 0.6 and accounts for the spreading of HNO_3 from an individual particle over the 21-s "tailing" period by increasing the effective value of net NO_y used to determine D_{NAT}. Net NO_y' is the value of net NO_y in ppbv that must be subtracted from net $NO_y(t_0)$ to account for the HNO_3 from particles sampled in the previous 20 s. Net NO_y' is given by:

$$\text{Net NO}_y' = \sum_{i=1}^{N} [\text{Net NO}_y(t_i) \times \bar{R}(t_0 - t_i)], \qquad (6)$$

where N is the number of peaks (interpreted as single large particles) in the 20 s interval before t_0 and net $NO_y(t_i)$ is the value of the ith peak recorded at time t_i. $\bar{R}(t_0 - t_i)$ is the fraction of HNO_3 released from the ith particle that contributes to the value net $NO_y(t_0)$ (Figure 12b). Only net $NO_y(t_0)$ peak values greater than 1 ppbv (10 times the instrument limit of detection) are counted as particles. Using equation (5), this corresponds to a minimum particle size of approximately 5 μm. The peaks in a selected interval of the net NO_y time series are evaluated individually and sequentially for particle sizes according to equations (5) and (6), yielding a size distribution for the data interval. The resulting size distribution using this method for the data interval in Figure 12a has a total number density less than 10^{-4} cm^{-3} (Figure 12c). Hence this method is useful for determining particle size distributions with very low number densities.

4.3. Numerical Simulation Method

[43] When the peak occurrence frequency in the net NO_y time series is greater than 0.15 s^{-1}, net NO_y values cannot be converted into particle sizes as in section 4.2 due to the likelihood of multiple particle sampling. Like the single particle analysis method, the numerical simulation procedure for higher number concentrations relies on the assumption that large particles are randomly distributed along the flight track segments. This assumption, coupled with the knowledge of how the NO_y instrument responds to the sampling of an HNO_3 particle (described by R, section 4.2), allows for a Monte Carlo simulation of the net NO_y time series that would result from sampling a particular particle size distribution. The representativeness of the assumed size distribution can be evaluated using net NO_y occurrence histograms for the simulated and actual data intervals. For reasonable statistical confidence, intervals of 500–1000 s should be chosen. The size distribution must be constant over the analysis interval for representative results. A necessary condition for this criteria to be met is that the average values of net NO_y and the standard deviation of net NO_y are relatively constant (±30%) over small time intervals (100 s) as is the case in Figure 13a. These criteria are not met for most analysis periods containing large

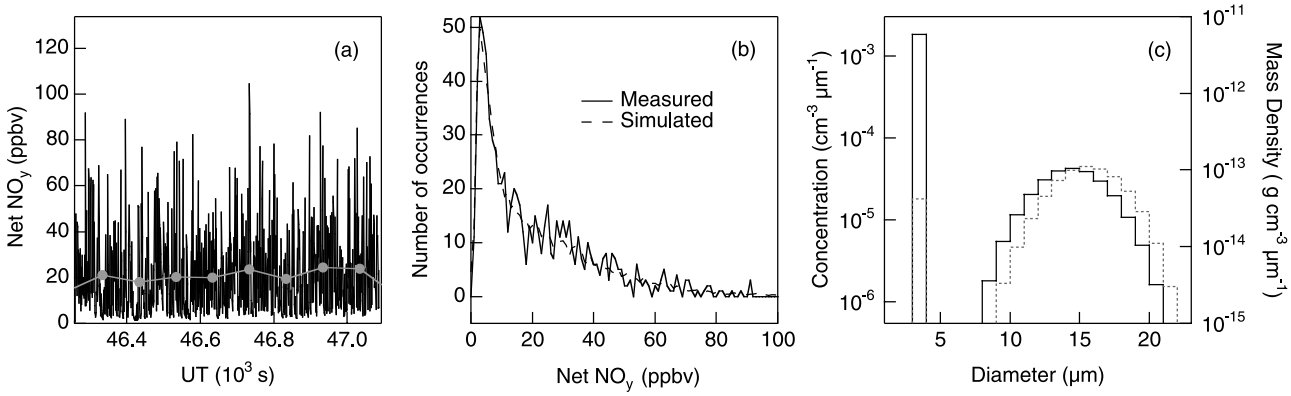

Figure 13. Numerical simulation method for determining particle size distributions (adapted from *Fahey et al.* [2001]). (a) Time series of approximately 800 s used in the analysis (20 January 2000, 46 287–47 086 UT). The data are 1-s average values. The gray circles indicate average net NO_y values calculated over 100-s intervals. (b) Occurrence histograms for measured (solid line) and modeled data (dashed line) intervals. (c) Resulting size distribution expressed as volume density (black solid line), and mass density (gray dotted line).

particles in the SOLVE/THESEO 2000 data set. Thus the use of the numerical simulation method is limited in this data set.

[44] The numerical simulation procedure for determining particle sizes and concentrations from the net NO_y time series is shown in Figure 13. This numerical procedure has been described previously by *Fahey et al.* [2001]. The first step of the procedure is to compute the average net NO_y value for the analysis interval. The second step is to simulate the response of the NO_y instrument sampling a population of spherical NAT particles with an assumed size distribution randomly dispersed along a notional flight track. The number concentration of the assumed particle distribution is scaled so that the simulated time series has the average observed net NO_y value. The HNO_3 released from each particle that is "sampled" is distributed along 21 s of the notional net NO_y time series according to the function R. The simulated net NO_y time series interval results from the superposition of released HNO_3 from all sampled particles. The third step is to compare the simulated time series to the actual net NO_y time series using net NO_y occurrence histograms for each data interval (Figure 13b). Finally, the assumed size distribution is manually adjusted in iterative steps, changing the mean diameter and width of the distribution until the difference between the two occurrence histograms is minimized. The fitting procedure does not necessarily return a unique size distribution describing the sampled particle population. The size distribution for the net NO_y data interval in Figure 13a is bimodal with a small mode below 5 μm and a large mode at 14 μm diameter (Figure 13c).

4.4. Probability Method

[45] For data intervals where the 100-s average values of net NO_y are rapidly changing and the peak occurrence frequency is greater than 0.15 s^{-1}, there is no ideal method for determining particle size distributions. For this situation, the method of maximum likelihood is used for estimating the most probable particle size present along a segment of the flight track (see Figure 14). In this method, the first step is to compute the average net NO_y value for the analysis interval. The short data interval (8 s) shown in Figure 14a

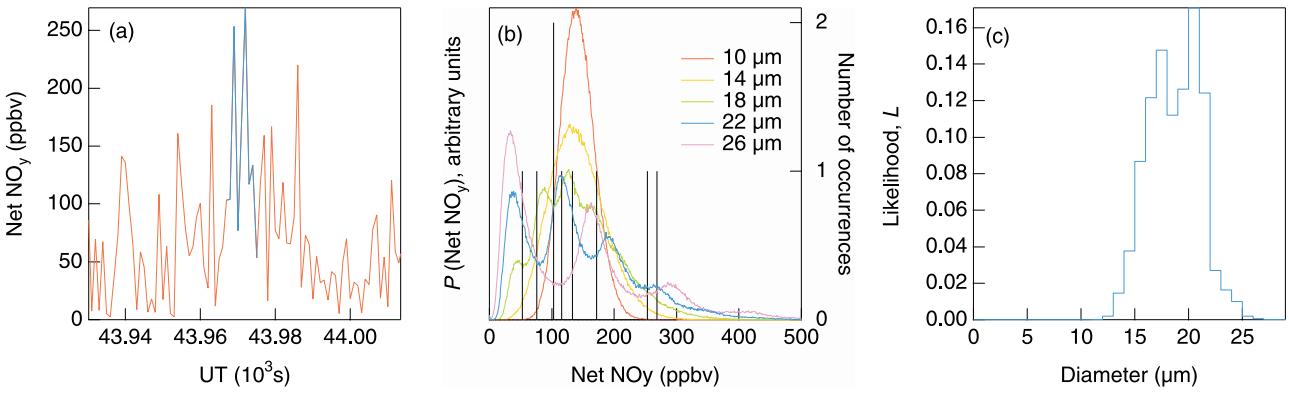

Figure 14. Maximum likelihood method for determining the most probable particle sizes along the flight tracks. (a) Time series of 8 s used in the analysis (31 January 2000, 43 967–43 975 UT). (b) Normalized probabilities for selected particle diameters (left) and histogram of net NO_y occurrence (right) for blue highlighted data in Figure 14a. (c) Resulting likelihood as a function of particle diameter.

has an average net NO_y value of 142 ppbv. Second, a series of numerical simulations of extended periods ($>10^5$ s) as described in section 4.3 is performed using the average net NO_y value of the data interval of interest and an assumed particle distribution containing a single particle size. Each simulation run produces a net NO_y occurrence histogram that would be observed if the average value of net NO_y were produced by a randomly dispersed population of that single particle size. Simulations are run for sizes in 1-μm steps between 5 and 30 μm diameter. When normalized to one, each histogram is equivalent to a probability distribution function, $P([\text{net } NO_y]_i;\{D_{NAT}\})$ which defines the probability that a value of net NO_y will be produced by sampling particles of the single size D_{NAT}. It is important to run the simulation for long periods at the designated average net NO_y value ($>10^5$ s) to produce a smooth probability distribution function. A selected number of probability functions for the data interval in Figure 14a is shown in Figure 14b. Next, an occurrence histogram is generated for the data interval of interest (Figure 14b). Finally, the relative likelihood that the set of observed net NO_y values, $\{[\text{net } NO_y]_i\}$, was produced by particles of each single size D_{NAT} is calculated. The likelihood, L, that particles of size D_{NAT} produced the time series interval of observations is calculated by the product of the probabilities $P([\text{net } NO_y]_i;\{D_{NAT}\})$ over all occurrences, $\{[\text{net } NO_y]_i\}$, in the interval, and is given by:

$$L\{D_{NAT}\} = \prod_i^N P\left([\text{Net } NO_y]_i;\{D_{NAT}\}\right) \quad (7)$$

where N is the number of net NO_y values in the data interval of interest [*Bevington and Robinson*, 1992]. The resulting function, $L\{D_{NAT}\}$, represents the relative likelihood that the interval of observations was produced by particles of the size D_{NAT}. $L\{D_{NAT}\}$ for the data interval in Figure 14a is shown in Figure 14c. Typically, $L\{D_{NAT}\}$ is a Gaussian-like function, with the maximum value representing the most probable single NAT particle size that produced the net NO_y time series interval. For the data in Figure 14a, the maximum occurs at about 18 μm diameter.

[46] The most probable size can be derived for a net NO_y data interval of any length. Because all values of $P([\text{net } NO_y]_i;\{D_{NAT}\})$ are less than one, the product of a large number of probabilities is a very small number. Thus, when analyzing long data intervals (>50 s), it is numerically more convenient to maximize the natural logarithm of the likelihood function, so that the product in equation (7) becomes a sum.

4.5. Results

[47] Particle sizes were evaluated in 1000-s data bins using the single particle detection method for low peak occurrence frequency (<0.15 s^{-1}) and the probability method for high peak occurrence frequencies (>0.15 s^{-1}). The most probable particle sizes determined by these two methods are indicated in the time series plots of Figure 7. The 1000-s intervals of the flight track containing fewer than 10 particles (number concentrations $<4 \times 10^{-6}$ cm^{-3}) were not considered in the analysis. This excludes all of the 1000-s data intervals during the flight of 7 March. Figure 15a summarizes the most probable particle sizes for all seven flights in equivalent latitude space (P. Newman, personal communication, 2000), where a value of 90 °N is defined as the center of the vortex [*Nash et al.*, 1996]. The edge of the vortex for these seven flights occurs at an equivalent latitude of approximately 65 °N [*Popp et al.*, 2001]. Figure 15b shows approximate particle concentration versus equivalent latitude for each 1000-s interval. In the hatched region of the graph, particle concentrations are likely to be higher than reported values due to the multiple particle sampling effect described in section 4. As expected from the large-particle signals shown in Figures 7 and 8, most probable particle sizes and concentrations are higher for the midwinter sampling period than for the late winter period. The data show no

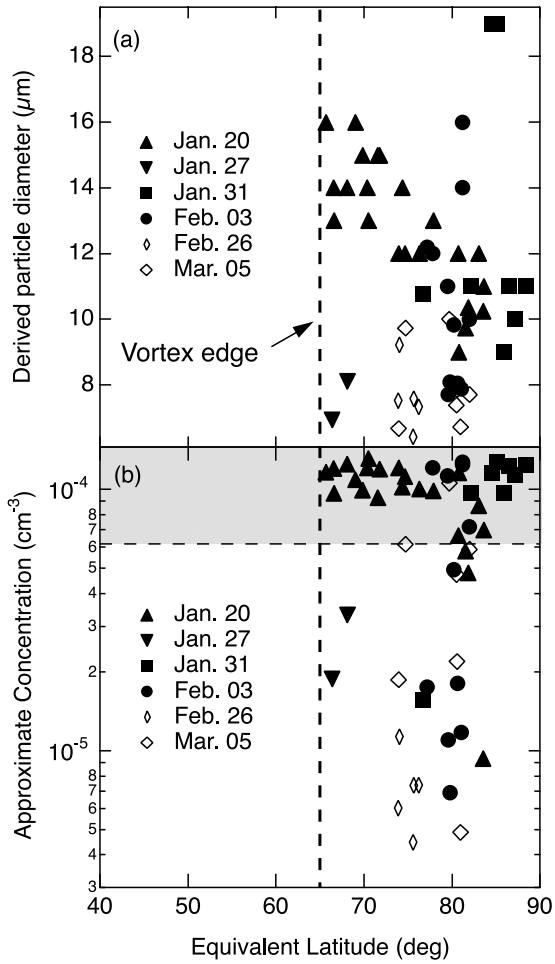

Figure 15. Summary of particle size and concentration results. In both panels, the closed symbols represent data taken between 20 January and 3 February 2000, and the open symbols represent data taken between 26 February and 7 March 2000. The gray dashed vertical line marks the edge of the vortex as determined by *Popp et al.* [2001]. (a) Derived particle diameter versus equivalent latitude for all flights and for all 1000-s intervals of the flight track where large particles were observed. (b) Approximate particle concentration (1000-s interval averages) versus equivalent latitude for all flights. Values inside the hatched region are lower limits due to multiple particle sampling.

preferred location of particles between 65 and 90 °N equivalent latitude, with particles existing near the edges as well as in the core of the vortex.

[48] Results of the size determination methods (sections 4.2–4.4) have been intercompared for several data intervals. For example, a probability analysis of the data interval shown in Figure 13a yields the most probable particle size as 14 μm. This result is consistent with the numerical simulation results of *Fahey et al.* [2001] shown in Figure 13c. In addition, the probability distribution functions (such as those in Figure 14b) for single size particle populations were compared to the occurrence histogram of the actual data interval shown in Figure 13b. In this comparison, the minimum difference was achieved between the 14-μm data interval probability distribution function and the actual data net NO_y occurrence histogram. Similarly, for the single particle detection method example given in Figure 12, the probability analysis yields a most likely size of 9 μm, the same value given by the peak of the size distribution in Figure 12c. Additional numerical simulation analyses have been performed for selected intervals of the data set and are consistent with the results presented by *Northway et al.* [2002, Table 1]. These simple tests demonstrate strong consistency between the particle sizing methods used in this analysis.

4.6. Uncertainties

[49] The NO_y measurements are accurate to about ± 15% with a limit of detection less than 0.1 ppbv [*Fahey et al.*, 1989]. Using equation (2), the absolute uncertainty in the NO_y measurements results in an uncertainty for calculated particle diameters of approximately ± 5%. Additional uncertainties for the different particle sizing methods are described below.

4.6.1. Uncertainty in the single particle detection method

[50] Uncertainty in size determinations using this method is based primarily on the agreement between the two NO_y channels which was less than 5% for the SOLVE/THESEO 2000 flight data used here. A 5% error in the channel agreement will produce up to a 10% error in the size determinations of the smallest particles (5 μm diameter) using equations (5) and (6). The calculated sizes for larger particles are affected less by the channel agreement. The 5% uncertainty in the channel agreement also affects how accurately R describes the actual response of the NO_y instrument to HNO_3-containing particles. The assumption of an average arrival time of a sampled particle to the detector, (i.e. the use of the average function, $\bar{R}$), results in an estimated 20% uncertainty for an individual particle diameter calculation. This results in an overall uncertainty for the size distribution in Figure 12c of ± 1μm for the smallest and largest size bins.

4.6.2. Uncertainty in the numerical simulation method

[51] For this method, the uncertainty will depend in general on the distribution of HNO_3 mass over the observed size range (Figure 13c). The histogram fitting process for the interval in Figure 13a is more sensitive to the large mode of the size distribution than the small mode, since it contains more HNO_3 mass. Shifting the large mode of the size distribution ± 2 μm results in a substantially poorer histogram fit. Hence the results for the large mode in Figure 13c are quite robust. By contrast, shifting (± 2 μm) or changing the magnitude (± 30%) of the small mode of the size distribution only moderately degrades the fit. Thus the number and size of the particles in the small mode are significantly uncertain. In addition, the fitting procedure is less sensitive to the addition of particles to the assumed size distribution between the large and small modes (4–6 μm).

[52] Quantification of the small mode in Figure 13c is strongly affected by R. The function R is used to distribute the HNO_3 from all sizes of particles over the 21-s response time. Small changes in R cause large changes in the apparent abundance of particles in the small mode. Furthermore, the small mode is very sensitive to the level of agreement between the two NO_y channels in the absence of particles because the simulation uses the difference signal, net NO_y. The large size mode, by contrast, is only weakly affected by R and the channel agreement.

4.6.3. Uncertainty in the probability method

[53] The likelihood function is typically Gaussian in form, and the uncertainty in the most likely size is estimated by the change in D_{NAT} necessary to change the maximum of the likelihood function L, by $e^{-1/2}$ [*Bevington and Robinson*, 1992]. For the probability distribution in Figure 14c, this corresponds to an uncertainty in the most likely size of ± 3 μm. For the 1000-s data intervals discussed in section 4.7, the uncertainty given by the distribution is less than 1 μm.

4.7. Discussion

[54] During the midwinter sampling period, most probable large particle sizes for 1000-s data intervals ranged from 6 to 20 μm diameter. The largest observed particles of approximately 20 μm on 31 January, are consistent with the largest particles predicted by the growth model results shown in *Fahey et al.* [2001] and *Carslaw et al.* [2001]. Although most probable particle sizes for the late winter period (5–10 μm) are only a few μm smaller in diameter than those observed during the midwinter period, average net NO_y values and particle concentrations are significantly less than those measured during the late winter period. Since particle volume is proportional to $(D_{NAT})^3$, these particles contain significantly less HNO_3 and are much less important for denitrification.

[55] The differences in large particle sizes and concentrations observed during the midwinter as compared to the late winter sampling period must be due to differences in particle nucleation or growth conditions, or a combination of these factors. Particles sedimenting during the late winter period most likely experienced lower S_{NAT} profiles due to previous denitrification events, thereby slowing growth rates. As discussed above, minimum temperatures during the two sampling periods likely influenced the extent of particle growth and nucleation. Also, denitrification of this winter was highly spatially inhomogeneous [*Popp et al.*, 2001], so particles observed during the late winter period likely experienced much more variable S_{NAT} conditions than those observed earlier in the winter. Thus, as particles sedimented and advected from the point of nucleation, they could have grown and partially evaporated, leading to smaller diameters at the sampling point.

[56] Three-dimensional models incorporating the nucleation, growth, and sedimentation of large particles are needed

to better understand the differences in particle populations between the two sampling periods seen in Figure 15. However, direct comparisons of our data and modeling results are not straightforward. Aspects of the net NO_y measurement described in this paper make it impossible to fully derive from the data the quantities of total condensed HNO_3 and particle sizes along the flight tracks. As shown here, many sections of the net NO_y time series do allow for the determination of these quantities. Many atmospheric models have relatively low spatial resolution as compared to the net NO_y measurement. However, in comparing to such models, it is not meaningful to average particle sizes and the amount of condensed HNO_3 along the flight track over long segments of the flight tracks, because there is a great deal of variability in these quantities (Figure 7). The following comparisons are recommended in using the net NO_y data to evaluate the simulation of large-particle distributions by atmospheric models: (1) Compare the model output with Figure 6 to see if particles greater than 2 μm are predicted in the correct geographic locations; (2) Compare relative amounts of net NO_y predicted by the model for different flight days and flight altitudes with the data in Figure 7. The enhancement factors in Figure 3 could be used in conjunction with the data in Figure 7 to compare net NO_y mixing ratios along the flight track with modeled amounts of condensed HNO_3. (3) Finally, if comparisons (1) and (2) yield promising results, more detailed comparisons could be achieved by simulating net NO_y values using modeled size distributions and comparing them to actual net NO_y data with occurrence histograms.

5. Conclusions

[57] In situ measurements of NO_y contained in large particles were obtained over widespread areas of the 1999/2000 Arctic vortex during the SOLVE/THESEO 2000 campaign. The data provide a unique opportunity to constrain PSC processes related to stratospheric denitrification. This study establishes a basis for analyzing large-particle clouds derived from the NO_y measurements. The primary conclusions of this work are as follows:

1. The NO_y signal from large (>2 μm) HNO_3-containing particles was measured across widespread areas of the 1999/2000 Arctic vortex. The observations spanned a period of 48 days from 20 January to 7 March. The observations presented here demonstrate that large HNO_3-containing particles were a persistent feature of the 1999/2000 Arctic winter.

2. Particles were detected using the difference signal (net NO_y) between two NO_y measurements made at separate locations on a particle separator mounted on the ER-2 aircraft. The sampling characteristics of the NO_y instrument are such that individual HNO_3-containing particles with ambient concentrations less than about 10^{-4} cm^{-3} and sizes greater than approximately 5 μm can be individually resolved within the net NO_y time series. The observed particles are assumed to be composed of NAT or NAD. The equilibrium HNO_3 composition of STS particles is too low to cause the observed net NO_y time series.

3. During the midwinter sampling period (20 January to 3 February), large particles were detected in a significant portion of the inner vortex air parcels between 15 and 21 km as sampled by the NO_y instrument. The range of particle populations varied substantially over the period with the greatest particle signals measured on 20 and 31 January and 3 February. On these flights large particles were typically observed in the coldest parts of the vortex, and they were sometimes absent near the vortex edge. On the flights during the late winter period (26 February to 7 March), large-particle signals were lower and less frequent. No particles were detected in the Arctic vortex during the last three ER-2 flights made between 7 and 16 March.

4. Large particles were typically observed at temperatures less than 198 K. The associated supersaturation with respect to NAT (S_{NAT}) was estimated as an upper limit to be between 1 and 100, suggesting ongoing particle growth at the time of sampling. In addition, the air up to 4 km above the sampled large-particle clouds also was typically saturated with respect to NAT. During the late winter period, regions of NAT saturation above the ER-2 flight track were smaller than they were during the midwinter period, suggesting a possible explanation for the reduced large-particle signals measured in the later period. Because of long growth and evaporation times and large fall velocities associated with large particle sizes, local S_{NAT} values greater than unity are not a sufficient condition to predict the presence of large particles. Large particles must nucleate and begin sedimentation and advection at altitudes well above the sampling point.

5. Particles were occasionally observed in air subsaturated with respect to NAT ($S_{NAT} < 1$) suggesting ongoing particle evaporation. Thus conditions of local subsaturation with respect to NAT cannot be used to predict the absence of large particles in air parcels. Typically, large particles require a day or longer to evaporate at temperatures 1 or 2 degrees above T_{NAT}, whereas smaller 2 or 3-μm particles would evaporate more quickly at these temperatures. Observations of large particles in air with $S_{NAT} < 1$ provide additional evidence that the observed peaks in the difference NO_y signal are due to single large particles and not "packets" of many smaller particles.

6. The nucleation mechanism for large NAT particles is unknown. The reported low number concentrations and large particle sizes imply that a selective nucleation mechanism leads to the formation of large particles. Analysis of the meteorological fields suggests that synoptic-scale ice saturation conditions did not play a large role in the nucleation and formation of the observed large particles.

7. Particle populations were characterized using three analytical methods. With the single particle detection method, peaks in the net NO_y time series are individually evaluated and converted to NAT particle diameters. The use of this method demonstrates the NO_y instrument as a sensitive detector for low number density particle populations (total number density < 10^{-4} cm^{-3}). When the NO_y instrument is sampling more than one particle on average during the instrument 1-s sampling period (total number density > 10^{-4} cm^{-3}), a numerical simulation is used to derive size distributions. In order to use this method, the particle distribution must be relatively constant over a period of 500 to 1000 s. Lastly, when both high and rapidly changing large-particle signals prevent the determination of size distributions using the aforementioned methods, the most probable particle size can be calculated for any net NO_y data interval. The analyses presented here of particle sizes and concentrations, particularly for particles in the 2–6 μm

diameter range, are limited by the accuracy of the derived function, *R*. *R* is the derived time-dependent response of the NO_y instrument to HNO_3 release and is particularly sensitive to systematic differences between the two NO_y measurements. The results obtained demonstrate strong consistency between the three different particle sizing methods.

8. The three methods described above were used to determine particle sizes and concentrations for portions of seven flights in the Arctic polar vortex. Derived large particle sizes range from 5 to 20 μm diameter and number concentrations range from 10^{-5} cm^{-3} to 10^{-3} cm^{-3}. Particle sizes were smaller and concentrations were lower during the late winter period as compared to the midwinter period.

[58] Large particles were an important feature of the 1999/2000 Arctic winter, and they likely played a role in the observed widespread denitrification. The widespread existence of large particles, especially those larger than 10 μm in diameter, requires that large regions of the vortex are saturated with respect to NAT. Thus it is likely that particles do not form in the stratosphere of warmer Arctic winters. This is consistent with the absence of denitrification in such winters. In the Antarctic, however, temperatures are lower and widespread denitrification is thought to occur every year. Therefore it is likely that large particles are a characteristic feature of Antarctic winters as well as very cold Arctic winters such as the 1999/2000 winter. In addition, synoptic-scale ice formation may play a more important role in Antarctic denitrification. In the future, Arctic winters may become more similar to Antarctic winters if the stratosphere cools due to increased levels of greenhouse gases [*Shindell et al.*, 1998; *Waibel et al.*, 1999].

[59] Although the SOLVE/THESEO 2000 mission provided valuable PSC data, questions about nucleation and denitrification will likely remain unanswered until more observations are obtained. In particular, the nucleation mechanism(s) that allows for NAT or NAD particle populations as low as 10^{-5} cm^{-3} to exist over widespread areas of the vortex is still unknown. The relationship between large-particle formation and denitrification is beginning to be quantified in a three-dimensional model [*Davies et al.*, 2002]. Accurate information about large-particle sampling locations and conditions and size distributions presented here should provide valuable constraints for atmospheric models that attempt to represent the PSC nucleation process and calculate vortex denitrification in Arctic winters. Many opportunities exist for further studies of the chemical and physical processes of large HNO_3-containing particles using this data set.

[60] **Acknowledgments.** The authors wish to thank the NASA ER-2 pilots J. Barrilleaux, J. Nystrom, and D. Porter and ground crew; Richard Winkler for his programming assistance; and Rich McLaughlin for assistance with Figure 2. This work was supported by the NASA Upper Atmosphere Research Program. Work at the Jet Propulsion Laboratory, California Institute of Technology, was carried out under contract with the National Aeronautics and Space Administration. Some of the material presented is based upon work supported by the National Science Foundation under award ATM-9871353, P. Wennberg, P.I.

References

Bevington, P. R., and D. K. Robinson, *Data Reduction and Error Analysis for the Physical Sciences*, 2nd ed., McGraw-Hill, New York, 1992.

Biermann, U. M., T. Presper, T. Koop, J. Mößinger, P. J. Crutzen, and T. Peter, The unsuitability of meteoritic and other nuclei for polar stratospheric cloud freezing, *Geophys. Res. Lett.*, *23*, 1693–1696, 1996.

Carslaw, K. S., B. P. Luo, S. L. Clegg, T. Peter, P. Brimblecombe, and P. J. Crutzen, Stratospheric aerosol growth and HNO_3 gas phase depletion from coupled HNO_3 and water uptake by liquid particles, *Geophys. Res. Lett.*, *21*, 2479–2482, 1994.

Carslaw, K. S., B. P. Luo, and T. Peter, An analytic expression for the composition of aqueous HNO_3-H_2SO_4 stratospheric aerosols including gas phase removal of HNO_3, *Geophys. Res. Lett.*, *22*, 1877–1880, 1995.

Carslaw, K. S., T. Peter, and S. L. Clegg, Modeling the composition of liquid stratospheric aerosols, *Rev. Geophys.*, *35*, 125–154, 1997.

Carslaw, K. S., M. Wirth, A. Tsias, B. P. Luo, A. Dörnbrack, M. Leutbecker, H. Volkert, W. Renger, J. T. Bacmeister, and T. Peter, Particle microphysics and chemistry in remotely observed mountain polar stratospheric clouds, *J. Geophys. Res.*, *103*, 5785–5796, 1998.

Carslaw, K. S., J. A. Kettleborough, M. J. Northway, S. Davies, R.-S. Gao, D. W. Fahey, D. Baumgardner, M. P. Chipperfield, and A. Kleinböhl, A vortex-scale simulation of the growth and sedimentation of large nitric acid hydrate particles, *J. Geophys. Res.*, *107*, 10.1029/2001JD000467, in press, 2002.

Davies, S., et al., Modeling the effect of denitrification on Arctic ozone depletion during winter 1999/2000, *J. Geophys. Res.*, *107*, 10.1029/2001JD000445, in press, 2002.

Del Negro, L. A., et al., Evaluating the role of NAT, NAD, and liquid H_2SO_4/H_2O/ HNO_3 solutions in Antarctic polar stratospheric cloud aerosol: Observations and implications, *J. Geophys. Res.*, *102*, 13,255–13,282, 1997.

Denning, R. F., S. L. Guidero, G. S. Parks, and B. L. Gary, Instrument description of the Airborne Microwave Temperature Profiler, *J. Geophys., Res.*, *94*, 16,757–16,765, 1989.

Deshler, T., and S. J. Oltmans, Vertical profiles of volcanic aerosol and polar stratospheric clouds above Kiruna, Sweden: Winters 1993 and 1995, *J. Atmos. Chem.*, *30*, 11–23, 1998.

Dessler, A. E., J. Wu, M. L. Santee, and M. R. Schoeberl, Satellite observations of temporary and irreversible denitrification, *J. Geophys. Res.*, *104*, 13,993–14,002, 1999.

Dhaniyala, S., K. A. McKinney, and P. O. Wennberg, Lee-wave clouds and denitrification in the polar stratosphere, *Geophys. Res. Lett.*, *29*, 10.1029/2001GL013900, 2002.

Drdla, K., A. Tabazadeh, R. P. Turco, M. Z. Jacobson, J. E. Dye, C. Twohy, and D. Baumgardner, Analysis of the physical state of one Arctic polar stratospheric cloud based on observations, *Geophys. Res. Lett.*, *21*, 2475–2478, 1994.

Dye, J. E., B. W. Gandrud, D. Baumgardner, K. R. Chan, G. V. Ferry, M. Loewenstein, K. K. Kelly, and J. C. Wilson, Observed particle evolution in the polar stratospheric cloud of January 24, 1989, *Geophys. Res. Lett.*, *17*, 413–416, 1990.

Fahey, D. W., K. K. Kelly, G. V. Ferry, L. R. Poole, J. C. Wilson, D. M. Murphy, M. Loewenstein, and K. R. Chan, In situ measurements of total reactive nitrogen, total water, and aerosol in a polar stratospheric cloud in the Antarctic, *J. Geophys. Res.*, *94*, 11,299–11,315, 1989.

Fahey, D. W., K. K. Kelly, S. R. Kawa, A. F. Tuck, M. Loewenstein, K. R. Chan, and L. E. Heidt, Observations of denitrification and dehydration in the winter polar stratospheres, *Nature*, *344*, 321–324, 1990.

Fahey, D. W., et al., The detection of large HNO_3-containing particles in the winter Arctic stratosphere, *Science*, *291*, 1026–1031, 2001.

Gao, R. S., et al., Partitioning of the reactive nitrogen reservoir in the lower stratosphere of the Southern Hemisphere: Observations and modeling, *J. Geophys. Res.*, *102*, 3935–3949, 1997.

Gao, R. S., et al., Observational evidence for the role of denitrification in Arctic statospheric ozone loss, *Geophys. Res. Lett.*, *28*, 2879–2882, 2001.

Goodman, J., S. Verma, R. F. Pueschel, P. Hamill, G. V. Ferry, and D. Webster, New evidence of size and composition of polar stratospheric cloud particles, *Geophys. Res. Lett.*, *24*, 615–618, 1997.

Hanson, D., and K. Mauersberger, Laboratory studies of the nitric acid trihydrate: Implications for the south polar stratosphere, *Geophys. Res. Lett.*, *15*, 855–858, 1988.

Herman, R. L., et al., Hydration, dehydration, and the total hydrogen budget of the 1999/2000 winter Arctic stratosphere, *J. Geophys. Res.*, *107*, 10.1029/2001JD001257, in press, 2002.

Hofmann, D. J., and T. Deshler, Stratospheric cloud observations during formation of the Antarctic ozone hole in 1989, *J. Geophys. Res.*, *96*, 2897–2912, 1991.

Kleinböhl, A., et al., Vortexwide denitrification of the Arctic polar stratosphere in winter 1999/2000 determined by remote observations, *J. Geophys. Res.*, *107*, 10.1029/2001JD001042, in press, 2002.

Kondo, Y., H. Irie, M. Koike, and G. E. Bodeker, Denitrification and nitrification in the Arctic stratosphere during the winter of 1996–1997, *Geophys. Res. Lett.*, *27*, 337–340, 2000.

Koop, T., U. M. Biermann, W. Raber, B. P. Luo, P. J. Crutzen, and T. Peter, Do stratospheric aerosol droplets freeze above the ice frost point?, *Geophys. Res. Lett.*, *22*, 917–920, 1995.

Manney, G. L., and J. L. Sabutis, Development of the polar vortex in the 1999–2000 Arctic winter stratosphere, *Geophys. Res. Lett.*, *27*, 2589–2592, 2000.

May, R. D., Open-path, near-infrared tunable diode laser spectrometer for atmospheric measurements of H_2O, *J. Geophys. Res.*, *103*, 19,161–19,172, 1998.

McIntyre, M. E., The stratospheric polar vortex and sub-vortex: Fluid dynamics and midlatitude ozone loss, *Philos. Trans. R. Soc. London Ser. A.*, *352*, 227–240, 1995.

Middlebrook, A. M., M. A. Tolbert, and K. Drdla, Evaporation studies of model polar stratospheric cloud films, *Geophys. Res. Lett.*, *23*, 2145–2148, 1996.

Molina, M. J., R. Zhang, P. J. Wooldridge, J. R. McMahon, J. E. Kim, H. Y. Chang, and K. D. Beyer, Physical chemistry of the $H_2SO_4/HNO_3/H_2O$ system: Implications for polar stratospheric clouds, *Science*, *261*, 1418–1423, 1993.

Nash, E. R., P. A. Newman, J. E. Rosenfield, and M. R. Schoeberl, An objective determination of the polar vortex using Ertel's potential vorticity, *J. Geophys. Res.*, *101*, 9471–9478, 1996.

Neuman, J. A., L. G. Huey, T. B. Ryerson, and D. W. Fahey, Study of inlet materials for sampling atmospheric nitric acid, *Environ. Sci. Technol.*, *33*, 1133–1136, 1999.

Northway, M. J., P. J. Popp, R. S. Gao, J. C. Holecek, D. W. Fahey, G. C. Toon, and T. P. Bui, Relating inferred HNO_3 flux values to the denitrification of the 1999–2000 Arctic vortex, *Geophys. Res. Lett.*, *29*, 10.1029/2002GL015000, in press, 2002.

Peter, T., Microphysics and heterogeneous chemistry of polar stratospheric clouds, *Annu. Rev. Phys. Chem.*, *48*, 785–822, 1997.

Poole, L. R., and M. P. McCormick, Airborne lidar observations of Arctic polar stratospheric clouds: Indications of two distinct growth stages, *Geophys. Res. Lett.*, *15*, 21–23, 1988.

Popp, P. J., et al., Severe and extensive denitrification in the 1999–2000 Arctic winter stratosphere, *Geophys. Res. Lett.*, *28*, 2875–2878, 2001.

Richard, E. C., et al., Severe chemical ozone loss inside the Arctic polar vortex during winter 1999–2000 inferred from in situ airborne measurements, *Geophys. Res. Lett.*, *28*, 2197–2200, 1999.

Salawitch, R. J., G. P. Gobbi, S. C. Wofsy, and M. B. McElroy, Denitrification in the Antarctic stratosphere, *Nature*, *339*, 525–527, 1989.

Salcedo, D., L. T. Molina, and M. J. Molina, Homogeneous freezing of concentrated aqueous nitric acid solutions at polar stratospheric temperatures, *J. Phys. Chem. A.*, *105*, 1433–1439, 2001.

Santee, M. L., W. G. Read, J. W. Waters, L. Froidevaux, G. L. Manney, D. A. Flower, R. F. Jarnot, R. S. Harwood, and G. E. Peckham, Interhemispheric differences in polar stratospheric HNO_3, H_2O, ClO, and O_3, *Science*, *267*, 849–852, 1995.

Schreiner, J., C. Voigt, A. Kohlmann, F. Arnold, K. Mauersberger, and N. Larsen, Chemical analysis of polar stratospheric cloud particles, *Science*, *283*, 968–970, 1999.

Scott, S. G., T. P. Bui, K. R. Chan, and S. W. Bowen, The meteorological measurement system on the NASA ER-2 aircraft, *J. Atmos. Oceanic Technol.*, *7*, 525–540, 1990.

Shindell, D. T., D. Rind, and P. Lonergan, Increased polar stratospheric ozone losses and delayed eventual recovery owing to increasing greenhouse-gas concentrations, *Nature*, *392*, 589–592, 1998.

Sinnhuber, B.-M., et al., Large loss of total ozone during the Arctic winter of 1999/2000, *Geophys. Res. Lett.*, *27*, 3473–3476, 2000.

Smithsonian Institution, *Smithsonian Meteorological Tables*, 6th ed., *Smithson. Inst. Publ. 4014*, prepared by R. J., List, p. 350, Washington D.C., 1958.

Solomon, S., R. R. Garcia, F. S. Rowland, and D. J. Wuebbles, On the depletion of Antarctic ozone, *Nature*, *321*, 755–758, 1986.

Tabazadeh, A., M. L. Santee, M. Y. Danilin, H. C. Pumphrey, P. A. Newman, P. J. Hamill, and J. L. Mergenthaler, Quantifying denitrification and its effect on ozone recovery, *Science*, *288*, 1407–1411, 2000.

Tabazadeh, A., E. J. Jensen, O. B. Toon, K. Drdla, and M. R. Schoeberl, Role of the stratospheric polar freezing belt in denitrification, *Science*, *291*, 2591–2594, 2001.

Tolbert, M. A., and O. B. Toon, Solving the PSC mystery, *Science*, *292*, 61–63, 2001.

Toon, G. C., The JPL MkIV Interferometer, *Opt. Photonic News*, *2*, 19–21, 1991.

Toon, O. B., P. Hamil, R. P. Turco, and J. Pinto, Condensation of HNO_3 and HCl in the winter polar stratospheres, *Geophys. Res. Lett.*, *13*, 1284–1287, 1986.

Toon, O. B., R. P. Turco, and P. Hamill, Denitrification mechanisms in the polar stratospheres, *Geophys. Res. Lett.*, *17*, 445–448, 1990.

Voigt, C., et al., Nitric acid trihydrate (NAT) in polar stratospheric clouds, *Science*, *290*, 1756–1758, 2000.

Waibel, A. E., T. Peter, K. S. Carslaw, H. Oelhaf, G. Wetzel, P. J. Crutzen, U. Pöschl, A. Tsias, E. Reimer, and H. Fischer, Arctic ozone loss due to denitrification, *Science*, *283*, 2064–2069, 1999.

Wilson, J. C., M. R. Stolzenburg, W. E. Clark, M. Lowenstein, G. V. Ferry, and K. R. Chan, Measurements of condensation nuclei in the airborne Arctic stratospheric expedition: Observations of particle production in the polar vortex, *Geophys. Res. Lett.*, *17*, 361–364, 1990.

Wofsy, S. C., R. J. Salawitch, J. H. Yatteau, M. B. McElroy, B. W. Gandrud, J. E. Dye, and D. Baumgardner, Condensation of HNO_3 on falling ice particles: Mechanism for denitrification of the polar stratosphere, *Geophys. Res. Lett.*, *17*, 449–452, 1990.

World Meteorological Organization (WMO), *Scientific Assessment of Ozone Depletion, 1998*, Global Ozone Res. and Monit. Proj., Geneva, 1999.

Worsnop, D. R., L. E. Fox, M. S. Zahniser, and S. C. Wofsy, Vapor pressures of solid hydrates of nitric acid: Implications for polar stratospheric clouds, *Science*, *259*, 71–74, 1993.

Zhang, R., P. J. Wooldridge, and M. J. Molina, , *J. Phys. Chem*, *97*, 8541–8548, 1993.

Zondlo, M. A., P. K. Hudson, A. J. Prenni, and M. A. Tolbert, Chemistry and microphysics of polar stratospheric clouds and cirrus clouds, *Annu. Rev. Phys. Chem.*, *51*, 473–499, 2000.

T. P. Bui, Atmospheric Chemistry and Dynamics Branch, NASA Ames Research Center, Mail Stop 245-5, Moffett Field, CA 94035, USA.

K. S. Carslaw, School of the Environment, University of Leeds, Leeds LS2 9JT, UK.

S. Dhaniyala, R. C. Flagan, and P. O. Wennberg, California Institute of Technology, Mail Code 150-21, 1200 E. California Boulevard, Pasadena, CA 91125, USA.

D. W. Fahey, R. S. Gao, J. C. Holecek, M. J. Northway, and P. J. Popp, NOAA Aeronomy Laboratory, 325 Broadway, R/AL6, Boulder, CO 80305, USA. (northway@al.noaa.gov)

R. L. Herman, Jet Propulsion Laboratory, Mail Stop 183-401, 4800 Oak Grove Drive, Pasadena, CA 91109, USA.

L. R. Lait, Goddard Space Flight Center, National Aeronautics and Space Administration, Code 916, Greenbelt, MD 20771, USA.

M. J. Mahoney, Jet Propulsion Laboratory, Mail Stop 245-101, 4800 Oak Grove Drive, Pasadena, CA 91109, USA.

M. A. Tolbert, CIRES, University of Colorado, Campus Box 216, Boulder, CO 80309, USA.

G. C. Toon, Jet Propulsion Laboratory, Mail Stop 183-601, 4800 Oak Grove Drive, Pasadena, CA 91109, USA.